Evaluation of the NAQFC Driven by the NOAA Global Forecast System Version 16: Comparison with the WRF-CMAQ During the Summer 2019 FIREX-AQ Campaign

Youhua Tang[1,2], Patrick C. Campbell[1,2], Pius Lee[1], Rick Saylor[1], Fanglin Yang[3], Barry Baker[1], Daniel Tong[1,2], Ariel Stein[1], Jianping Huang[3,4], Ho-Chun Huang[3,4], Li Pan[3,4], Jeff McQueen[3], Ivanka Stajner[3], Jose Tirado-Delgado[5,6], Youngsun Jung[5], Melissa Yang[7], Ilann Bourgeois [8,9], Jeff Peischl [8,9], Tom Ryerson[9], Donald Blake [10], Joshua Schwarz [9], Jose-Luis Jimenez [8], James Crawford [11], Glenn Diskin[7], Richard Moore [7], Johnathan Hair [7], Greg Huey [11], Andrew Rollins [9], Jack Dibb [12], Xiaoyang Zhang[13]

1. NOAA Air Resources Laboratory, College Park, MD, USA.
2. Center for Spatial Information Science and Systems, George Mason University, Fairfax, VA, USA.
3. NOAA National Centers for Environmental Prediction, College Park, MD, USA
4. I.M. Systems Group Inc., Rockville, MD, USA
5. Office of Science and Technology Integration, NOAA National Weather Service, Silver Spring, MD, USA
6. Eastern Research Group Inc, USA
7. NASA Langley Research Center, Hampton, VA, USA
8. Cooperative Institute for Research in Environmental Sciences, University of Colorado Boulder, Boulder, CO, USA
9. NOAA Chemical Sciences Laboratory, Boulder, CO, USA
10. Department of Chemistry, University of California at Irvine, Irvine, CA, USA
11. School of Earth and Atmospheric Sciences, Georgia Institute of Technology, Atlanta, GA, USA
12. Earth Systems Research Center, University of New Hampshire, Durham, NH, USA
13. Department of Geography & Geospatial Sciences, South Dakota State University, Brookings, SD, USA

Correspondence: Youhua Tang (youhua.tang@noaa.gov)

Abstract

The latest operational National Air Quality Forecasting Capability (NAQFC) has been advanced to use the Community Multi-scale Air Quality (CMAQ) model version 5.3.1 with CB6r3 (carbon bond 6 revision 3)-Aero7 (version 7 of the aerosol module) chemical mechanism and is driven by the Finite Volume Cubed-Sphere (FV3)-Global Forecast System, version 16 (GFSv16). This update has been accomplished by development of the meteorological preprocessor, NOAA-EPA Atmosphere-Chemistry Coupler (NACC), adapted from the existing Meteorology-Chemistry Interface Processor (MCIP). Differing from the typically used Weather Research and Forecasting (WRF)-CMAQ system in the air quality research community, the interpolation-based NACC can use various meteorological outputs to drive CMAQ (e.g., FV3-GFSv16) even though they are in

1

different grids. In this study, we compare and evaluate GFSv16-CMAQ vs. WRFv4.0.3-CMAQ using observations over the contiguous United States (CONUS) in summer 2019 verified with surface meteorological and AIRNow observations. During this period, the Fire Influence on Regional to Global Environments and Air Quality (FIREX-AQ) field campaign was performed and we compare the two models with airborne measurements from the NASA DC-8 aircraft. The GFS-CMAQ and WRF-CMAQ systems have overall similar performance with some differences for certain events, species and regions. The GFSv16 meteorology tends to have a stronger diurnal variability of planetary boundary layer height (higher during daytime, and lower at night) than WRF over the U.S. Pacific coast, and it also predicted lower nighttime 10-m winds. In summer 2019, GFS-CMAQ system showed better surface O_3 than WRF-CMAQ at night over the CONUS domain; however, their PM2.5 predictions showed mixed verification results: GFS-CMAQ yielded better mean biases but poorer correlations over the Pacific coast. These results indicate that using global GFSv16 meteorology with NACC to directly drive CMAQ via the interpolation is feasible and yields reasonable results compared to the commonly-used WRF driving approach.

1. Introduction

Traditionally, mesoscale meteorological models such as the Weather Research and Forecasting Model (WRF) (Powers et al., 2017) are used as the meteorological drivers for air quality models (AQMs) on the same ("native") model grid, such as Community Multiscale Air Quality Model (CMAQ) (Byun & Schere, 2006). The NOAA National Weather Service's (NWS) National Air Quality Forecasting Capability (NAQFC) has historically used a different approach, in which the hourly meteorological outputs from prior operational models, such as North American Mesoscale Model (NAM), are interpolated to the CMAQ grid to drive its air quality prediction. Prior to this work, a "PREMAQ" coupler (Otte et al, 2004) combined both meteorological processing and Sparse Matrix Operator Kernel Emissions (SMOKE) (Houyoux et al., 2000) processes, such as point source plume rise effects. However, since the release of CMAQ version 5, the meteorology-dependent plume rise, sea salt, and dust emission processes are included as inline modules in CMAQ, and thus the corresponding emission processes are no longer needed in PREMAQ. Furthermore, PREMAQ has no built-in interpolator, and thus relied on external interpolators to remap the non-native-grid meteorological inputs, such as NAM, to the targeted CMAQ domain, though it did perform vertical layer collapsing/interpolation to reduce vertical layers for CMAQ. The interpolation approach allows more flexibility for using different meteorological data (i.e., besides just WRF) to drive CMAQ; however, there is potential to raise mass-consistency issues between models. It should be noted that the mass-consistency issues may also exist using native-grid couplers (Byun, 1999a, 1999b), which can stem from the original mass-inconsistent meteorological model outputs or due to the temporal interpolation of the meteorological data. The well-developed offline AQMs, such as CMAQ, have already considered such mass-consistency treatments using different meteorological inputs (Byun et al., 1999c).

To upgrade the NAQFC system with the latest CMAQ model and NOAA operational meteorology, we developed an updated interpolation-based meteorological coupler, the NOAA-EPA Atmosphere-Chemistry Coupler (NACC) (Campbell et al., 2022) adapted from the U.S. EPA's Meteorology-Chemistry Interface Processor (MCIP) version 5 (Otte and Pleim, 2010; https://github.com/USEPA/CMAQ). The NACC system replaced PREMAQ, and effectively couples the Finite-Volume Cubed-Sphere (FV3) Dynamical Core - Global Forecast System version 16 (GFSv16) (Yang et al., 2020; Harris et al, 2021) to CMAQ v5.3.1 (hereafter referred to as GFS-CMAQ). Campbell et al. (2022) described the development and application of the GFS-CMAQ system using NACC (in their work referred to as "NACC-CMAQ") and a comprehensive comparison between the current (GFS-CMAQ since July 20, 2021) and previous (NAM-CMAQv5.0.2) operational NAQFC model performances.

In this study, we analyze the impacts of the meteorological model drivers, and compare GFS-CMAQ using NACC interpolation to the commonly-used native-grid WRF-CMAQ application and its impact on air quality predictions in summer 2019. Yu et al. (2012a, 2012b) had previously compared the CMAQ performance driven by WRF-NMM and WRF-ARW during the 2006 TexAQS/GoMACCS field campaign, and found that the NMM-CMAQ and ARW-CMAQ showed overall similar performance with some differences for certain events, chemical species, and regions. Similarly, this study focuses on the comparison of GFS-CMAQ versus WRF-CMAQ (see Section 2, Methodology), and verifies the model performance against the aircraft observations from the Fire Influence on Regional to Global Environments and Air Quality (FIREX-AQ) field experiment during summer 2019 (Section 4). Surface verification is also performed using AIRNow data for August 2019 (Section 3), serving as a benchmark for the new NAQFC versus the traditional WRF-CMAQ used in the air quality modeling community. This study focuses on the period of summer 2019, and Campbell et al. (2022) evaluated the GFS-CMAQ for longer periods.

2. Methodology

Here we compare the two CMAQ (version 5.3.1) runs driven by the interpolated GFSv16 meteorology (GFS-CMAQ) and WRF meteorology (WRF-CMAQ). All other settings, such as emission and lateral boundary conditions are the same. The meteorology-related physics is discussed in the following sections to address the models' performance discrepancies. Both the GFS-CMAQ and WRF-CMAQ simulations are run from a period covering 12 July – 31 August, 2019, each using the last 10 days in July as the model spin-ups that are not included in the analyses.

2.1 GFS Meteorological Inputs

The GFSv16 is the current operational global forecast system in NOAA/NCEP using FV3 dynamical core. Its detailed configuration can be found in Campbell et al. (2022) and Yang et al.

1 (2020). Compared to the previous version (v15), GFSv16 updated many physical schemes (Table
2 1) and added the parameterization for sub-grid scale nonstationary gravity-wave drag. To use the
3 GFS's meteorology to drive CMAQ, a meteorological coupler, NACC, is developed (Campbell
4 et al., 2022). Differing from the original MCIP which was developed to process WRF/ARW
5 meteorology for CMAQ, the NACC coupler interpolates non-native-grid meteorology to a user-
6 defined grid and has parallel processing capability, which drastically reduces its run time for
7 operational forecasts (Campbell et al., 2022). Currently, NACC employs two horizontal
8 interpolation methods: bilinear and nearest-neighbor. In this study, we use the nearest-neighbor
9 method to categorical (discontinuous) variables that include land use types, vegetation fraction,
10 terrain elevation, Monin–Obukhov length, friction velocity, and soil temperatures, while the
11 bilinear interpolation is used for mainly smoothly varying (continuous) meteorological variables
12 that include wind fields, temperature, pressure, and specific humidity. The CMAQ model is
13 defined in the Arakawa C-grid (Arakawa and Lamb, 1977), and thus the GFSv16 horizontal wind
14 components (U, V) need to be interpolated to the perpendicular cell faces instead of the cell
15 center (Otte and Pleim, 2010) after rotation to the defined map projection. The scalar variables
16 are defined in the cell centers of the targeted grid, and thus their interpolations are more
17 straightforward: from GFSv16 A-grid to CMAQ A-grid. The NACC coupler can either use the
18 native layers or interpolate inputs to a set number of user-defined CMAQ vertical layers. The
19 GFSv16 has 127 vertical layers with global coverage in roughly 13 km horizontal resolution,
20 where the targeted CMAQ domain is in 12×12 km grids over the Contiguous United States
21 (CONUS) with 35 vertical layers (Campbell et al, 2022). Here we use 24-hour GFSv16 forecasts
22 starting at 12 UTC each day.
23
24 Most variables needed by CMAQ are directly interpolated from the GFSv16 hourly outputs. The
25 NACC processor has options to calculate diagnostic variables, such as planetary boundary layer
26 (PBL) height, if they are needed. In this study, we use the interpolated GFSv16's PBL height
27 instead of the diagnostic one. It also has an option to import the externally provided land-surface
28 variables. Here we import updated 2018–2020 climatological averaged leaf area index (LAI) and
29 NOAA near-real-time (NRT) greenness vegetation fraction (GVF) from satellite-based Visible
30 Infrared Imaging Radiometer Suite (VIIRS) retrievals (Campbell et al., 2022). The updated
31 satellite-based LAI and GVF impact CMAQ's biogenic emissions and dry deposition processes,
32 which were described in detail in Campbell et al. (2022).
33
34 **2.2 WRF Meteorology**

35 To compare with GFSv16 meteorology processed by NACC, a corresponding WRF version 4.0.3
36 (Skamarock et al, 2021) simulation is run covering the NAQFC's native grid, which is a 12 km
37 horizontal resolution with Lambert conformal map projection over CONUS. Table 1 shows the
38 WRF configuration, which is commonly employed in CONUS meteorological and air quality
39 studies in the community, versus the current NOAA/NWS operational global model GFSv16.
40 GFSv16 uses the NOAA/NCEP's Global Data Assimilation System (GDAS)

4

1 (https://www.emc.ncep.noaa.gov/data_assimilation/data.html) for its initial conditions and runs
2 on its own global dynamics and physics without any other constraints. The regional WRF
3 simulation uses GFSv16 for its initial conditions. In this study, GFSv16 was re-initialized with
4 GDAS every 24 hours, and WRF conducted the continuous run after its spin-up period.
5 Furthermore, WRF also takes its lateral boundary conditions from GFSv16 every 6 hours. For
6 the WRF run, we have enabled the four-dimensional data assimilation (FDDA) for the horizontal
7 winds, temperature, and humidity (Table 1) every 6 hours, thus nudging towards GFSv16. This
8 nudging method used in WRF runs can help reduce the difference of two meteorological models,
9 though its effect may vary depending on events as WRF and GFS use different physics.
10
11 WRF and GFSv16 have similar settings for the land surface model, surface layer and radiation
12 schemes; however, their microphysics and PBL schemes are different (Table 1). Compared to the
13 35-layer WRF with a 100 hPa domain top, GFSv16 has a much higher domain top (0.2 hPa) and
14 127 vertical layers, which are interpolated by NACC to 35 sigma layers up to 14 km for CMAQ.
15 We use NACC (inherited from MCIP version 5.0) to process WRF hourly meteorology, while
16 maintaining the 35-layer vertical layer structure. Thus, in contrast to GFS-CMAQ, the WRF-
17 CMAQ system uses the native grid without interpolation.
18
19 **2.3 CMAQ Configuration**

20 Here CMAQ version 5.3.1 (Appel et al., 2021) is used with the Carbon Bond 6 revision 3
21 (CB6r3; Yarwood et al., 2010, 2014; Luecken, et al., 2019) chemical mechanism and Aero7
22 treatment of secondary organic aerosols (CB6r3_AE7_AQ). CMAQ 5.3.1 includes a series of
23 scientific updates from the previous version (Appel et al., 2021), including the updated air-
24 surface exchange and deposition modules, which showed significant impact on ozone prediction
25 compared to the previous NAQFC (Campbell et al., 2022). We also include the bi-directional
26 NH_3 (BIDI-NH_3) exchange model for NH_3 surface fluxes. An updated Biogenic Emissions
27 Landuse Dataset v5 (BELD5) is used in this study to drive the inline Biogenic Emissions
28 Inventory System (BEIS) version 3.61. The anthropogenic emissions are provided by the
29 National Emissions Inventory Collaborative (NEIC) with base year 2016 version 1 (NEIC 2016).
30 We replace the U.S. EPA default CMAQ dust emissions model with an inline windblown dust
31 model known as "FENGSHA" (Fu et al., 2014; Huang et al., 2015; Dong et al., 2016). The
32 FENGSHA dust scheme uses the sediment supply map and magnitude of the friction velocity
33 (USTAR) compared to a threshold friction velocity (UTHR) to calculate the potential of dust
34 emission flux. The UTHR depends on the land cover, soil type (clay fraction), and soil moisture
35 Campbell et al. (2022).
36
37 We have updated the wildfire emissions system in CMAQv5.3.1 based on the Blended Global
38 Biomass Burning Emissions Product (GBBEPx) (Zhang and Kondragunta, 2006; Zhang et al.,
39 2011). The GBBEPx uses satellite-detected fire radiative power (FRP) to estimate wildfire
40 smoke emissions for a number of species: CO (carbon monoxide), NOx (nitrogen oxides), SO_2

5

(sulfur dioxide), elemental carbon, primarily emitted organic aerosols, and PM2.5. We derive the wildfire volatile organic compounds (VOC) emission from GBBEPx CO emission based on the emission ratios of FINN data (Wiedinmyer et al., 2011), and the splitting factors from the SMOKE model (Baker et al, 2016) are used to further split the total fire VOC emission to speciatied hydrocarbon emissions. The satellite FRP is estimated from satellite brightness temperature anomaly, and the GBBEPx processor assumes that the wildfire emissions are proportional to the FRP over certain landuse types in certain regions. The GBBEPx emissions are based on polar orbiting satellites: MODIS (Aqua and Terra satellites) and VIIRS (Suomi-NPP and NOAA-20 satellites) instruments, which are updated once per day. A wildfire emission preprocessor converts the GBBEPx emissions to CMAQ-ready input files using emission speciation and diurnal profiles (high during daytime and low at night) (adopted from U.S. EPA-based profiles) (Baker et al., 2016), and a daily scaling factor. Here we classify the wildfire into either a long-lasting fire (longer than 24 hours) or short-term fire (shorter than 24 hours) based on land use types and regions. As historic statistics shows that most fires (>95%) in east of 110°W last less than 24 hours, only the fires west of 110°W that have a model grid cell total forest fraction > 0.4 are assumed to be long-lasting fires All other short-term GBBEPx fires are assumed to have smoke emissions for 24 hours (i.e., day 1 only). Burning area could be highly uncertain as GBBEPx data do not include this information. One grid cell could have multiple fires and some big fire could appear in several grids. Here we carry the previous NAQFC's method, and apply a constant ratio: 10% of the grid cell, as the burning area (Pan et al., 2020) according to Rolph et al (2009).CMAQ treats wildfire emissions as point sources that undergo inline plume rise to distribute the smoke vertically. The default CMAQ plume rise used here is based on Briggs (1965), which is driven by fire heat flux (converted from FRP with a ratio of 1) and fixed burning area (assumed to be 10% of the $0.1° \times 0.1°$ grid cell).

3. Model Evaluations over the U.S. for August 2019

To first gain a general picture and compare the overall GFS-CMAQ and WRF-CMAQ model performances, in this section we evaluate the near-surface meteorological and air quality predictions during the FIREX-AQ August 2019 period against NOAA's METeorological Aerodrome Report (METAR; https://madis.ncep.noaa.gov/madis_metar.shtml) and the U.S. EPA's AirNow (https://www.airnow.gov/) observation networks. All the comparisons of meteorological variables are for those actually used in CMAQ. For GFS-CMAQ, it refers to the interpolated GFS data. Campbell et al (2022) included the detailed comparisons before and after interpolation, showing that the interpolated meteorology was very consistent with the original one. In this study, the model results are spatiotemporally interpolated to the corresponding observation locations for comparison.

3.1 Domain-Wide Meteorology against the METAR Network

Figure 1 shows the mean bias (MB) of interpolated GFS and WRF predicted surface meteorological variables compared to METAR data during August, 2019. Both meteorological models have a cool bias over the Western and Northeastern United States, and a warm bias over the western Rocky Mountain region and Southeastern United States (Figure 1a, 1b). Similar temperature predictions are expected since WRF uses the FDDA method nudging toward GFS data. However, GFS tends to be cooler than WRF over the Rocky Mountains and in the central and northeastern USA due to their different dynamics and physics. The GFSv16 cold bias in the lower troposphere is impacted by excessive evaporative cooling from rainfall (personal communication with NOAA/NCEP). Campbell et al. (2022) had detailed discussions about GFSv16 biases.

Both GFSv16 and WRF models have similar and rather significant dry biases for specific humidity (SH) predictions across CONUS (Figure 1c, 1d). Qian et al (2020) investigated this common dry bias in many models, and found that neglecting an irrigation contribution could cause this dry bias. Besides this issue, WRF's dry bias could also be affected by its nudging toward GFS, as GFS has widespread dry biases (Campbell et al. 2022). Their biases also have some noticeable differences over certain regions. For instance, WRF has less dry bias over Southern Texas than GFS.

Both models underestimate the mean 10-m wind speeds compared to METAR stations over the western U.S. WRF has stronger underpredictions over the Rocky Mountains and overpredictions over northeastern U.S., while GFS has stronger underpredictions over the Appalachian Mountains and overpredictions over Texas and Oklahoma. GFSv16's operational verification (https://www.emc.ncep.noaa.gov/gmb/emc.glopara/vsdb/v16rt2/g2o/g2o_00Z/index.html) also shows that it tends to underpredict the 10-m wind over the western U.S. during both daytime and nighttime, but shows overpredictions over the eastern U.S. Besides the difference of physical schemes etc. (Table 1), other possible reasons causing this surface wind difference could be effect of the gravity-wave drag (GFSv16 includes it, but the WRF run here does not), and vertical resolutions: GFS's 127 layers versus WRF's 35 layers, though they have similar vertical layers below 1km (Campbell et al, 2022). Some studies (Skamarock et al, 2019) revealed the necessity of fine vertical resolution for atmospheric simulations, especially within the PBL, near tropospheric top, and during convective events. Insufficient vertical resolution could also cause plume dilution on chemical transport modeling (Zhuang et al., 2018). The gravity-wave drag is also known to influence the synoptic-scale dynamics on the atmospheric flow over irregularities at the earth's surface such as mountains and valleys, and uneven distribution of diabatic heat sources associated with convective systems (Kim et al., 2003). Its parameterization is needed for large-scale models.

1 There are strong regional variabilities in the monthly mean PBL height differences between GFS
2 and WRF during normal daytime (represented by 18 UTC) and nighttime (represented by 06
3 UTC) (Figure 2). During daytime, GFS has a higher PBL height compared to WRF over the U.S.
4 Pacific coast, northern Rocky Mountains, northeastern and southeastern U.S., but it becomes
5 lower over the central U.S. (e.g., Texas, Oklahoma, and Kansas). At night, however, most of
6 these regional differences between GFS and WRF are reversed. This diurnal difference is
7 mainly driven by the different PBL schemes employed in GFS (Han and Bretherton, 2019) and
8 WRF (i.e., YSU) and the associated other physical suites, including the land surface data. So this
9 PBL difference has strong regional variations depending on geographic differences. The GFS's
10 PBL height has a strong diurnal variation over these regions, including the western and
11 northeastern U.S., and it shows a sharp rise and collapse after sunrise and sunset, respectively
12 (Campbell et al., 2022). These two selected times (18UTC and 06UTC) are not in the transition
13 periods for PBL's fast diurnal changes.
14

3.2 Evaluation of Regional Meteorology and Air Quality against the AirNow Network

16 The U.S EPA AirNow network provides hourly observations of near-surface ozone, fine
17 particulate matter (PM2.5), and meteorology. Campbell et al. (2022) showed detailed verification
18 of GFS-CMAQ with the surface AIRNow data. Here we focus on the difference between the
19 interpolation-based GFSv16 versus WRF downscaling and the impacts on meteorological and
20 chemical model performances. Figure 3 shows a comparison of these two models over two
21 specific regions, the U.S. West (CA, OR and WA) and Northeast states (CT, DE, MA, MD, ME,
22 NH, NJ, NY, PA, RI, VT and District of Columbia) (Figure S1), where the two models have
23 relatively large differences for some meteorological variables. GFS and WRF predict very
24 similar 2-m temperatures over the Pacific coast states: Washington, Oregon and California, and
25 both of them had similar cool bias (around 1K), R and RMSE (Figure 3a). However, these two
26 models show significant differences for the 10-m wind speed prediction over the Pacific coast
27 (Figure 3c), where WRF overpredicts the wind speed, especially at night and in later August.
28 Most AIRNow stations are located near urban or suburban areas, which generally have weaker
29 10-m wind speed than those at the METAR aviation weather stations near airports. For this
30 reason, although Figure 1e and 1f shows that GFS and WRF underpredict monthly-mean wind
31 speed over the METAR stations in the West, they still tend to overpredict wind (Figure 3c) over
32 AIRNow stations, especially for the WRF 10-m wind speed at night. Considering that the model
33 grid cells represent 12×12 km^2 averages, the true model-observation comparisons likely fall
34 somewhere between the urban/suburban AIRNow stations and METAR stations, depending on
35 the landuse fractions of each grid. Obviously the representation characteristics of observations
36 could affect the verification results. Compared to AIRNow observations, GFSv16 has overall
37 better scores for surface wind speed predictions over the U.S. West, where the WRF's larger
38 surface wind speed overprediction is associated with its PBL height predictions (Figure 3e, 3f).
39 During the nighttime, GFS has a lower PBL height (10–50% lower than WRF) and weaker
40 vertical mixing, which tends to bring less momentum flux from the upper layers to the surface,

8

and lead to lower nighttime wind and better agreements with the AIRNow wind-speed observation.

Over the northeast, the mean bias (MB) of GFS temperature is about -1K, while the WRF has a smaller, slightly positive MB of about 0.22K (Figure 3b). However, the GFS's temperature prediction has a better correlation coefficient, R, and RMSE, implying that it better captures some events, such as the 28–29 of August. Both models overpredict 10-m wind speeds in the northeast, but the GFS model yields better results due to a slightly lower PBLH at night (Figure 3f) than WRF that had significant overpredictions, especially during 25–29, August (Figure 3d) when the tropical storm Erin approached this region. Especially on 28 of August, when the storm was centered near the east coast of North Carolina, WRF significantly underpredicted 2-m temperature (Figure 3b) and overpredicted 10-m wind speed (Figure 3d). In the west around the same period, the tropical storm Ivo appeared in the southwest of the Baja California peninsula, and brought heavy rainfall in Mexico. Associated with this storm, a low pressure system expanded over most of the U.S. West. Differing from GFSv16, which is designed for the operational meteorological forecast, the WRF configuration used in this study is normal for driving CMAQ, but not tuned for storm weather prediction.

Figures 4a and 4b show the ozone predictions of the two models over these two regions, and GFS-CMAQ yields predominantly lower O_3 than WRF-CMAQ, especially at night. Over the west, the lower ozone in GFS-CMAQ is associated with their PBL height difference. First, with a certain dry deposition velocity between the models, it is easier to deplete ozone given the smaller volume of a shallower PBL. Second, the shallower PBL results in higher surface NOx concentrations (not shown) and ozone titration rates near NOx source regions, and consequently lower ozone there at night. Last, the lower PBL could decouple from the residual layer, and result in weaker or no vertical ozone exchange with the residual layer at night (Caputi et al, 2019). All these factors contribute to the lower nighttime ozone of GFS-CMAQ compared to WRF-CMAQ. Since GFS-CMAQ already underpredicts ozone due to combined meteorological factors, such as the temperature underprediction (Figure 4a), the GFS-CMAQ's further ozone reduction (possibly due to its lower PBLH at night) exacerbates its low bias. However, over the Northeast, the similar impacts help the GFS-CMAQ yield much better MB due to its better agreement with the observed nighttime low ozone over the Northeast. Over the entire CONUS domain, the situation is similar: for an average August 2019, the GFS-CMAQ has a lower ozone MB (1.1 ppb) compared to WRF-CMAQ (4.7 ppb). Figure 5 shows that both models have similar daytime ozone prediction over CONUS. However, GFS-CMAQ better captures low nighttime ozone over the U.S. East than WRF-CMAQ (Figure 5c, 5d).

GFS-CMAQ has substantially higher PM2.5 mean concentrations over the U.S. West, but lower over the U.S. Northeast compared to WRF-CMAQ (Figures 4c, 4d). These model differences are also related to their interpolated GFSv16 versus downscaled WRF meteorological drivers.

Because both models use the same emissions under relatively clean background conditions in the west (i.e., prevailing westerly flow from the Pacific Ocean), the PBL and wind speed differences have significant impacts on their near-surface pollutant concentrations, especially at night. Both models show strong PM2.5 diurnal variations (high at night and low during daytime), driven by the meteorological diurnal variation (e.g. PBL), which overcomes the emission diurnal variation (usually high during daytime and low at night). Compared to WRF-CMAQ, GFS-CMAQ has lower nighttime PBL height and weaker wind speed at night, which leads to weaker vertical mixing and venting, and increases the pollutant concentrations near the surface and yields higher surface PM2.5 over the U.S. West (Figure 4c). Its higher surface PM2.5 could also result in stronger local dry deposition. In contrast to local vertical mixing and venting effects on PM2.5 discussed above, there are strong (and potentially counterbalancing) impacts of model PBL and horizontal wind speed differences on downstream PM2.5 concentrations at night. WRF-CMAQ's deeper PBL and stronger wind speeds at night (Figures 3c–3f) tends to transport aerosols and their precursors more efficiently downstream via the dominant advection pathway. Figure 6 shows that these monthly mean background PM2.5 differences appear in East of Rocky Mountain (WRF-CMAQ is about 2 μg/m^3 higher) during both daytime and nighttime. This effect is very prominent in the Northeast region. Although both models predicted similar PM2.5 magnitude over the U.S. Northeast, GFS-CMAQ yields the overall PM2.5 underprediction, and its monthly-mean PM2.5 is 2.6 μg/m^3 lower than the WRF-CMAQ prediction (Figure 4d). Especially during 01–09 August, WRF-CMAQ had about 4 μg/m^3 higher surface PM2.5 background than that of GFS-CMAQ. In this case, the WRF-CMAQ model has a better agreement with observations (Figure 4d). It is possible that the GFS-CMAQ's nighttime PBL heights (wind speeds) are too shallow (weak) in this case, which does not allow enough transport of pollutants to the downstream (Eastern USA). Overall, GFS-CMAQ and WRF-CMAQ have mixed performances for PM2.5 predictions during the August 2019 period: GFS-CMAQ has better PM2.5 prediction over the U.S West, and WRF-CMAQ yields better results over east of Rocky mountain (Figure 6).

4   Model Comparisons against the FIREX-AQ Aircraft Data

From late July to early September, 2019, the joint NOAA-NASA FIREX-AQ field campaign (https://csl.noaa.gov/projects/firex-aq/) employed a suite of satellites, aircraft, vehicles and ground site platforms aimed to observe, analyze, and characterize air pollutants emitted from wildfire sources over the CONUS (Ye et al., 2021). The FIREX-AQ airborne measurements provide a three-dimensional dataset from various meteorological, gas, and aerosol instruments that can be used to verify the GFS-CMAQ and WRF-CMAQ model performance, while elucidating reasons for any model differences. Here the focus of the FIREX-AQ model comparison and verification is against observations taken primarily from the NASA DC-8 aircraft, which include meteorological variables, gaseous and aerosol concentrations, and aerosol optical properties merged in one-minute temporal resolution. The model data are spatiotemporally interpolated to the flight paths for comparison. The majority of the FIREX-AQ

10

flights were over the western United States, and sampled within environments that both were *and* were not (see section 4.1) influenced by wildfire emissions (https://daac.ornl.gov/MASTER/guides/MASTER_FIREX_AQ_JulySept_2019.html). During a cluster of major wildfire events (see Section 4.2), the DC-8 sampled both near-source and aged smoke plumes between 02–08 August, 2019 (i.e., the Williams Flats, Snow Creek, and Horsefly Fires) across the states of Idaho, Washington, and Montana.

4.1 Comparison of the July 22 non-wildfire event over the central California Valley

On 22 July, the DC-8 aircraft flew from California to Boise, Idaho, while maintaining a relatively low-altitude (<1 km) above sea level (ASL) over the California Central Valley (Figure 7). This flight was not impacted by any major wildfire event, and was mainly controlled by anthropogenic emissions and local meteorological conditions. Figure 7 shows that the GFSv16 and WRF models had similar meteorological temperature and humidity predictions, and that both models have dry and warm biases over the Central Valley at lower altitudes (Figures 7d–7e) (Yun et al., 2020). GFS's horizontal wind speeds tend to have a stronger variability than WRF (Figure 7b), especially in high altitudes. For wind direction, WRF shows a better prediction than GFS around 20 and 24 UTC (Figure 7c).

Both GFS-CMAQ and WRF-CMAQ underestimate the vertical wind (W) variability by at least one order of magnitude, and WRF-CMAQ has weaker W variability than that of GFS-CMAQ, especially in high altitudes (Figure 7f). The model vertical velocities are not directly from the GFS or WRF model, but rather they are re-diagnosed in CMAQ to conserve mass (Otte and Pleim, 2010), and thus represent the whole layer's vertical movement across the 12 km by 12 km grid cell. With its flight speed around 80 to 240 m/s, the DC-8 aircraft's one-minute average sampling frequency results in an approximate 4.8 to 14 km horizontal scale, respectively, which is comparable to the 12 km CMAQ model resolution. The aircraft observations, however, include turbulence effects during its one-minute averages, which may not be temporally resolved by the models at this resolution. Thus, both the GFS-CMAQ and WRF-CMAQ vertical velocities are much lower and have almost no correlation with the aircraft observations.

Although both GFS-CMAQ and WRF-CMAQ have reasonable comparisons for most meteorological variables, including the horizontal winds, it continues to be a challenge to compare them with the observed vertical velocities. Thus to further elucidate the model vs. observation differences in vertical motions, Figure 8 shows a curtain plot of vertical velocities along the flight path from the two models. Since WRF-CMAQ remains in a native grid, its wind fields tend to be more balanced and have lower variability compared to the GFS-CMAQ wind fields. The stronger variability in W for GFS-CMAQ could be caused by GFS's non-hydrostatic dynamics or CMAQ's effort to counteract mass inconsistency effects from the interpolated horizontal wind fields (Byun, 1999b). Our comparison shows that the first factor should be the major one (Figure S2) for this event, as the GFS-CMAQ diagnosed W is very similar to that

11

from the original GFSv16 around 1km above the ground. As the original GFSv16 has similarly
stronger vertical velocities than the original WRF, the W difference between GFS-CMAQ and
WRF-CMAQ is unlikely due to interpolation error of horizontal winds.

GFS-CMAQ and WRF-CMAQ overall yield similar results for specific chemical species during
this DC-8 flight (Figure 9). Both models underestimate CO, O_3 and ethane (C_2H_6) concentrations
over the lower altitudes in the California Central Valley. Over the same flight segment, they have
better NOx (NO + NO_2) and ethene (C_2H_4) predictions, implying that the emissions of these two
species have better accuracy than those of CO and ethane. Figure 9f shows that the two models
also underestimate NOz (NOy–NOx), or the oxidized nitrogen species besides NOx, indicating
that the photochemical ozone production may also be underestimated. NOz is a good indicator of
the ozone photochemical formation (Sillman et al., 1997), where the O_3/NOz ratio represents the
ozone photochemical efficiency per NOx oxidation products. Thus, NOz and O_3 are typically
highly correlated over regions with active photochemical production. Our later analysis shows
that the models tend to underestimate certain hydrocarbons, such as ethane, which is likely
linked to O_3 and NOz underestimations, since the hydrocarbons are photochemical precursors of
O_3 and NOz.

The two models show slight differences in peak values of CO, ethene, and NOx around 23:30
UTC, where the GFS-CMAQ predicted concentrations are slightly higher and closer to
observations (Figure 9). These differences are due to their PBL predictions (both from the
corresponding meteorological model outputs), where GFS-CMAQ has a lower PBL height and
weaker emission vertical dilution compared to WRF-CMAQ (Figure 8). GFS-CMAQ tends to
underpredict O_3 more (Figure 9b), however, due to its higher NOx titration. This implies that the
effects of the transport and non-local transformation of O_3 could be stronger than that of local
precursor emissions. WRF-CMAQ has higher NOz (Figure 9f), but lower NOx compared to
GFS-CMAQ due to the time lag of O_3 and NOz photochemical formation. Consequently, the
peak O_3 values may not be well correlated with the emitted precursors, such as NOx and VOC.
Furthermore, the modeled peak C_2H_6 and C_2H_4 concentrations do not occur at the same time
around 23:30 UTC, while observations indicate that these two species should be highly
correlated in this region. This model mismatch implies that the VOC speciation factors for a
certain area or emission sector need to be improved over Southern California.

4.2 Comparison of the 6 August wildfire events over the U.S. Northwest

On 06 August, the DC-8 observed a cluster of three wildfires: the Williams Flats Fire (47.98 °N,
118.624 °W, 80 km to the northwest of Spokane, Washington), Snow Creek Fire (47.703°N,
113.4°W, 32 km northeast of Condon, Montana), and Horsefly Fire (46.963 °N, 112.441°W, 24
km east of Lincoln, Montana). Figure 10a shows the flight path on that date, where the DC-8
aircraft departed from Boise, ID, flew over the Williams Flats Fire region, then flew to Montana
to sample the Snow Creek and Horsefly Fires (i.e., Montana Fires), and finally returned to the

12

Boise base. The aircraft flew below 8 km for most flight segments near the fire plumes. Figure
S3 shows the corresponding GOES-16 satellite true color image, where these 06 August fires and
associated smoke plumes are visible and can be distinguished from the cloud bands to the south
that move northward later that day (Figure S3). The Williams Flats Fire was ignited by
lightning, and was the largest fire event sampled during the FIREX-AQ campaign burning from
about 02–08, August, 2019.

Both models significantly underpredicted CO (Figure 10c), submicron (aerosol diameter < 1μm)
organic aerosol (Figure 10e) and aerosol optical extinction coefficient (AOE) (Figure 10f), which
suggests an issue with the GBBEPx gas and aerosol emissions. The models performed well for
NO_2 during the Williams Flats and Montana Fires Fire below 6 km ASL, but there were
prominent underestimations for the high-altitude flight segments (Figure 10d). However, since
the NO_2 instrument (The NOAA NOyO3 4-channel chemiluminescence) had its NO_2 detection
limit around 0.01 ppb
(https://airbornescience.nasa.gov/sites/default/files/documents/NOAA%20NOyO3_SEAC4RS.p
df), the models might not truly underestimate NO_2 for these flight segments with extremely low
NO_2.WRF-CMAQ predicted higher O_3 values than the GFS-CMAQ, which overall agreed better
with observations for the Williams Flats Fire (Figure 10b). However, for the Montana Fires (~
23–24 UTC), WRF-CMAQ has higher O_3 biases and GFS-CMAQ yields better results. The
difference in O_3 is largely driven by the regional background concentration difference between
the two models, where WRF-CMAQ tends to have higher domain-wide O_3 concentrations than
GFS-CMAQ due to the meteorological effects discussed in section 3 even though they used the
same lateral boundary conditions.

Figure S4 shows the spatial overlay comparison of vertically averaged GFS-CMAQ predictions
at 21 UTC and the DC-8 flight observations for the altitude 1–3 km above ground level (AGL),
on 6 August, 2019. The peak NO_2 observation around 118.5°W, 48°N indicates the general
location of the Williams Flats fire. The GBBEPx emission and GFS-CMAQ prediction showed
shifted peak-value locations driven by the westerly modeled winds. For this flight, the GBBEPx
had stronger NOx fire emissions over two Montana locations than that over Williams Flats. The
model overpredicts the column averaged NO_2 concentrations, especially over the Montana fires,
which can not be reflected by the point-by-point NO_2 comparison result in Figure 10d. For this
flight, the mean GFS-CMAQ NO_2 along the flight path for 1–3km AGL is about 0.125 ppbv
compared to the observed mean NO_2 of 0.169 ppbv, and the model indeed showed a NO_2
underprediction along the flight path. However, in this case, the flight path did not encounter the
locations with modeled peak NO_2 values as the model misplaced the plumes, especially over the
Montana fires leading to this inconsistency. For ozone comparison (Figure S4b), this
inconsistency could also exist, though not as significant as for the high-gradient NO_2
concentrations. In the GFS-CMAQ prediction, the high ozone concentrations are almost co-
located with high NO_2 concentration (Figure S4b), but the observation did not show this feature.

13

Instead, some high-O_3 flight segments had relatively low NO_2 concentrations, such as those circled in the black rectangle box of Figure S4b. The observed NOx titration was not able to be produced by the 12 km models. Wang et al (2021) used a 100m-horizontal-resolution large eddy simulation and demonstrated the capability of using such techniques to capture some high-resolution features of fire plumes and associated chemical behavior. While such high resolution techniques are not currently feasible for the operational NAQFC, they demonstrate the limitation of using regional scale (12×12 km) models to capture such fine-scale features of the fire plume.

GFS-CMAQ has higher wildfire-related CO, NO_2, OA and AOE values that are closer to observations than WRF-CMAQ for the Montana Fires between 23–24 UTC at flight altitudes of ~ 4–5 km (Figure 10c–10f). Since these two models use the same GBBEPx emissions and wildfire plume rise algorithm (Briggs, 1965), the differences should be due to other reasons. To help explain these model differences, Figure 11a and 11b show the Differential Absorption High Spectral Resolution Lidar (DIAL-HSRL) retrieved aerosol backscatter coefficients (ABC) aboard the DC-8 aircraft without and with cloud screen, respectively. It shows that the major fire plumes of the William Flats Fire were below 4 km (~ 19–22 UTC) , but the Montana Fires (~23–24 UTC) extended from the surface up to 6 km, with some detached plumes reaching 10 km. The model predicted AOEs have an overall similar pattern, with major plumes below 4 km for the Williams Flats Fire (Figures 11c and 11d). Over the Montana Fires, the GFS-CMAQ predicts a slightly higher PBL height, thus allowing for the fire plume to reach a higher height near the DC-8 cruising altitude. In contrast, the WRF-CMAQ wildfire plumes are slightly lower than the aircraft flight path around 23–24 UTC, which leads to underpredictions of the fire emitted species (Figure 11d).

An interesting feature in the DIAL observations is the detached plume from 8 km to 10 km altitude (Figure 11a), where some cirrus clouds existed, and the DIAL retrieval could not distinguish whether they are pure clouds or clouds mixed with elevated aerosols above 8km. The cloud-screening image (Figure 11b) mainly showed the enhanced aerosols below 7km and some scattered signals near the high cloud edges. Cloud mixing with aerosols was usual for fire induced clouds, or pyrocumulonimbus (Peterson et al., 2021). Although in this event, the middle-size fires did not show evident of inducing the high-altitude clouds, the indicator of mixed clouds and aerosols in high altitudes still existed: both in-situ measured OA (Figures 10e) and AOE (Figure 10f, 11c, 11d) showed the enhanced aerosols around 25 UTC (or 1 UTC of the next day) above 8km. This elevated plume was generally captured by the GFS-CMAQ simulation, while underestimating its strength (Figure 11c); however, this feature was completely missed in WRF-CMAQ (Figure 11d). Considering the altitude range of the detached plume, the major model disparities are likely due to model convection differences in the free troposphere. To further investigate this impact, Figures 11e and 11f show curtain plots of RH predicted by the two models. GFS-CMAQ yields higher RH at such altitudes (10 km) compared to WRF-CMAQ around 23–24 UTC, indicating that the GFS-CMAQ has a stronger convection. The CMAQ

14

model uses inputted meteorology to diagnose convection activity and drive its ACM2 convection scheme. This convective activity is apparent in GOES-16 satellite images (Figure S3), as more fractional clouds appeared ahead of the northward moving frontal band. Both the GFSv16 and WRF models used here *do not* consider the fire heat feedback effect, and thus their predicted convection and clouds are only driven by the synoptic weather conditions. If such synoptic-to-mesoscale weather models consider wildfire heat feedback effects, their predictions may result in stronger convection and help correct their underpredictions in PBL heights.

4.3 Statistical Results of Model Performances for FIREX-AQ

4.3.1 *Meteorological Statistics*

During the FIREX-AQ field campaign, the DC-8 aircraft performed more than 20 flights over CONUS with detailed observations of various chemical compounds. Tables 2 and 3 show the statistical results of mean bias (MB), normalized mean bias (NMB), root mean square error (RMSE), correlation coefficient (R), and linear regression/slopes for the two models' performance over the western U.S. (west of 110°W) only at low altitudes (<3km ASL) for both non-fire and fire flight segments. The FIREX-AQ aircraft data included the smoke flag to mark the sampling times associated with fire plumes, identified by carbon monoxide and aerosol enhanced over background levels in downwind areas of specific fires. This smoke flag is used to distinguish the flight segments with and without fire influences. Most of these flights departed from Boise, ID, except the 22 July flight that flew from California to Idaho. As a result, they mainly flew over Idaho and its surrounding regions. The GFS tends to have a slightly higher wind speed with positive MB, while WRF has a small negative wind speed bias. Most of the DC-8 flights are during the daytime, and the GFS has a higher daytime wind speed than WRF at low altitudes. The GFS and WRF have very similar temperature predictions. For the RH, the GFS predictions are slightly dryer than those of WRF, especially for non-fire events. The meteorological models do not consider wildfire heat effects, and thus may have (in part) led to slightly warm MB for the non-fire events (Table 2) and slightly cool MB for the fire events (Table 3). Because both the GFSv16 and WRF models have similar MB shifts from an average temperature overprediction (Table 2; non-fire events) to an underprediction (Table 3; wildfire events), we can estimate that the fire effects make roughly a 1–2 Kelvin temperature enhancement to the background along the DC-8 flight paths below 3 km. This estimate assumes that the model temperature biases are generally representative of the western U.S. (west of 110°W), and are independent of the averaged flight segments that have different locations and periods in Table 2 and Table 3. Correspondingly, the air masses are dryer in the sampled wildfire plumes, as shown by the large reduction in the RH underpredictions (i.e., negative MBs) from Table 2 to Table 3.

4.3.2 *Chemical Statistics for Flight Segments without Fire Influences*

15

For most chemical species, the two models also have similar performance, indicating that the emissions and chemistry are major driving forces. For flight segments not encountering fire plumes, both models overpredict NOx, HNO_3, toluene, EC, and ammonium (NH_4^+), but underestimate PAN, benzene, C_2H_2, SO_2, and submicron sulfate and organic aerosols (OA) (Table 2). The SO_2 and submicron sulfate underprediction may be impacted by underestimated NEIC2016v1 SO_2 emissions over the western U.S. Since point sources, including power plant emissions, are the SO_2 sources, this comparison implies that the point sources for 2019 events have large uncertainties.

Although the models agree well with NOy observations, they disproportionately underestimate NOz (non-NOx reactive nitrogen species, or NOy-NOx) as shown by the regression slopes and MBs. The NOx and NOy observations have different missing data, and NOz is calculated when both NOx and NOy observations are available at certain sampling times. Due to the different sample number issues, their observed averages may not exactly match well (averaged NOx+NOz $\neq$ NOy in observations) though their corresponding modeled relationship are well balanced. Gaseous NOz species can be split into inorganic NOz (HNO_3, HONO, HNO_4, NO_3, $ClNO_3$, N_2O_5 et al.) and organic NOz, such as PAN, methyl peroxyl acetyl nitrate (MPAN) and RNO3 (or NTR, the other organic nitrate) et al. The precursors of organic NOz include hydrocarbons. One of the important organic NOz species is PAN, and both models underestimate PAN for the flight segments without fire influences (Table 2). PAN's carbonyl precursors include acetaldehyde (CH_3CHO) (44% of the global source), methylglyoxal (30%), acetone (7%), and a suite of other isoprene and terpene oxidation products (19%) (Fischer et al., 2014). CH_3CHO and acetone are also underestimated (Table 2), which help explain PAN's underestimation. For the oxidized hydrocarbons, like aldehydes (HCHO, CH_3CHO), their main atmospheric sources come from the oxidation of highly reactive VOCs, including alkanes, alkenes, and aromatics, instead of direct emissions (Parrish et al., 2012). So, the underestimations of HCHO and CH_3CHO are associated with the underestimations of their precursor hydrocarbons, including anthropogenic and biogenic VOCs. Our internal comparison with some limited surface VOC observations indicated that BEIS tends to underpredict biogenic emissions over the U.S. West, e.g. isoprene in Table 2. In this comparison, most anthropogenic hydrocarbons are disproportionately underestimated, except toluene, implying the VOC speciation issue in the NEIC2016v1 anthropogenic emissions (Table 2). A previous work discovered that a model overprediction in toluene was also related to the toluene speciation in the NEI emission inventory (Lu et al., 2020). In this comparison, both models tend to underpredict organic NOz, which is likely caused by the underestimation of certain VOCs.

Submicron ammonium (NH_4^+) and nitrate ion (NO_3^+) are also underestimated by both models during non-fire events (Table 2), suggesting there are NH_3 underestimates due to either insufficient NH_3 emissions or exaggerated NH_3 removal processes. There are, however, overpredictions in the intermediate species nitric acid (HNO_3), indicating the shift of gas-aerosol

16

1   equilibrium partition of the nitrate ion. It implies that the HNO_3 accumulates in the atmosphere
2   because the modeled NOx and inorganic NOz (such as NO_3) pathways toward the nitrate ion and
3   organic NOz are reduced due to underestimations of their other precursors (NH_3 and VOCs).
4
5   There are underestimations in the VOC and CO concentrations, which contributes to the ozone
6   underestimation during non-fire flight segments (Table 2). These non-fire comparisons also
7   highlight that both models have similar biases due to similar meteorology (Section 4.3.1), and
8   the use of the same anthropogenic emissions (NEIC2016v1), BEIS biogenic emission and
9   chemical models/mechanisms (i.e CMAQv5.3.1). The differences in the two models' bias, error,
10   and correlation/slope are much smaller than their individual magnitudes. As discussed above,
11   VOC speciation in the emission inventory could be one issue, as the model tends to overpredict
12   C_2H_4, but underestimate C_2H_2 and C_2H_6 etc. Some common biases over certain regions could be
13   related to certain common issues. For instance, some power plants supposed to shut down in the
14   original NEIC 2016 inventory might still emit pollutants during the flight observations, leading
15   to the disagreement of SO_2.
16
17   4.3.3 *Chemical Statistics for Flight Segments with Fire Influences*
18
19   The WRF-CMAQ and GFS-CMAQ models significantly underestimate CO, VOC, HONO, and
20   OA for fire-influenced flight segments at low altitudes (< 3 km) over the western U.S. (Table 3).
21   In conjunction with underestimated GBBEPx emissions during these wildfire events, other
22   possible causes for the average statistical underprediction are the CMAQ model's 12 km
23   horizontal resolution and the flight sampling coverage. Most of the fires that are averaged in the
24   statistics, such as the Horsefly (5.5 km^2 burning area) and Snow Creek Fires (7.3 km^2 burning
25   area), are at a much finer scale than the model grid. Only the largest Williams Flats Fire, with a
26   total burning area of 180 km^2 (Ye et al., 2021), had a comparable horizontal scale to the model
27   resolution.
28
29   The DC-8 aircraft had many flight segments near wildfire sources during the fire events in Table
30   3, and thus dilution of the emissions due to the relatively coarse model resolution may lead to
31   underestimations in the predicted slope for most wildfire emitted pollutants, such as CO and OA
32   (Table 3). The O_3 concentrations are also underestimated; however, the O_3 underpredictions are
33   reduced from the non-fire (Table 2) to fire events (Table 3). Abundant amounts of wildfire
34   emitted NOx can titrate ozone near the fire source region, and the models likely underestimate
35   these titration effects due to the 12 km model resolution (Figure S4). Thus, the models cannot
36   capture the strong spatial O_3 variability that is observed due to both reduction near source
37   regions and enhancement in downstream areas. Again, for this fire event comparison, both
38   models showed similar behavior and their differences were relatively smaller compared to the
39   overall model biases.
40

17

5. Summary and Discussion

The operational NOAA/NWS National Air Quality Forecasting Capability (NAQFC) recently underwent a major upgrade on July 20, 2021. The advanced NAQFC includes the recent Community Multi-scale Air Quality (CMAQ) model version 5.3.1 with CB6 (carbon bond version 6)-Aero7 (version 7 of the aerosol module) chemical mechanism, and is driven by the latest operational Finite Volume Cubed-Sphere (FV3)-Global Forecast System, version 16 (GFSv16) (Campbell et al., 2022). Here we analyze the impacts of the driving meteorological models on CMAQ model performance with the new GFSv16 interpolation-based meteorology versus the commonly-used native-grid Weather Research and Forecasting (WRF) model version 4.0.3 meteorology. The meteorological and chemical analysis includes both 2D ground-based and 3D aircraft measurements during the summer 2019, which encompasses the joint NOAA-NASA Fire Influence on Regional to Global Environments and Air Quality (FIREX-AQ) campaign. As CMAQ has existing mass conservation via adjustments of the contravariant vertical velocity (Otte and Pleim, 2010), the NACC interpolated GFSv16 wind field can be well handled in CMAQ (i.e., GFS-CMAQ).

The different NWS/NOAA operational GFS and commonly chosen WRF physics schemes employed in this study (Table 1) clearly have impacts on temperature, horizontal/vertical wind fields, PBL heights, and the corresponding CMAQ model predictions. During this study period over the U.S. West, both models showed moisture dry bias and temperature warm bias in low altitudes, which could be due to the issue mentioned by Qian et al (2020): the irrigation contribution being neglected (section 3.1), and impacts from soil moisture deficits on surface fluxes in both models. Due to their different physics, GFS has a stronger diurnal variation of PBL height, lower at night and higher during daytime over the U.S. West and Northeast. The differences in the GFS and WRF physics result in a larger impact than the difference between interpolated and native grids on the models' meteorological and air quality predictions, even despite using FDDA to nudge WRF simulation toward the GFSv16 data. Nudging toward observations or including data assimilation may yield different results for the WRF run, though they are not used here. In this study, FDDA nudging used in WRF to avoid growing errors across a continuous 1-month simulation. We note that if this method is turned off, the differences between GFSv16 and WRF predictions would have been even greater. This would further substantiate the dominance of using different model physics and their impacts on CMAQ model predictions. Campbell et al (2022) have the detailed comparisons for interpolated and original fields, and they are very consistent. In this study, we further compare the CMAQ vertical velocity diagnosed from the interpolated GFS horizontal wind, which is very consistent with the original GFS vertical velocity. Overall, the results of this study further corroborate the use of the GFSv16 data and NACC interpolation-based methods (Campbell et al., 2022) for regional CMAQ model applications in the scientific community.

18

Over CONUS, GFS-CMAQ demonstrated lower mean surface ozone (by about 3 ppb) and PM2.5 (by about 1 $\mu g/m^3$) than WRF-CMAQ in August 2019 (section 3). In the western U.S., the GFS has a stronger diurnal variability in PBL height and a better performance in nighttime 10-m wind speeds compared to WRF. The nighttime difference between these two models tends to be more significant than the corresponding daytime difference. Their difference is also impacted by both vertical/convective (mainly daytime) and upstream advective transport differences in GFS-CMAQ and WRF-CMAQ, which somewhat confounds the impact of different meteorological physics on chemical predictions from region to region. This transport effect is more significant on PM2.5 than that on O_3, as O_3 has a shorter lifetime and is more sensitive to local emissions in summer. In this study, neither GFS-CMAQ nor WRF-CMAQ show overwhelming performance advantage over the other, similar to the NMM-CMAQ and ARW-CMAQ comparison in Yu et al. (2012a, 2012b).

GFS-CMAQ and WRF-CMAQ demonstrated rather similar performance for major chemical variables during both FIREX-AQ non-fire (Table 2) and fire events (Table 3). Both models showed similar biases, indicating that other factors, including emissions, model resolution and chemistry etc. could be more important for the model predictions compared to the meteorological differences. The aircraft data comparison reveals many common issues in both model systems. One critical issue is whether the flight sampling coverage is comparable to the 12 km model resolution, especially for high-gradient fire emission, e.g. the case of 06 August flight (Figure S4). The observation representation issue also exists in other places, such as the near-surface meteorological comparison between AIRNow stations and METAR stations. Emission is the driving force for atmospheric composition concentrations. The comprehensive aircraft measurements help verify that the anthropogenic NEIC2016v1 inventory is overall reasonable, except for SO_2, NH_3 and certain hydrocarbons. The wildfire emission has bigger uncertainties, including the emission intensities, pollutant specification and plume rise, shown by the both models' results.

The NACC interpolation method is advantageous as it enables using the original meteorological driver directly via interpolation, and avoids running another model such as WRF to drive regional CMAQ applications. It is also faster, and more consistent with the original meteorological model (GFS) than using WRF even with nudging, since WRF's own physics could have stronger impact. In the current NOAA/NCEP operational GFS-CMAQ system, NACC only takes less than 5 minutes to process 72-hour data, which saves enough time for CMAQ to forecast extra 24 hours. These aspects can simultaneously benefit real-time forecasting and retrospective air quality applications in the scientific community. NACC can also adapt to quickly use any regional domain globally, and may also use other global meteorological data including reanalysis products. This helps mitigate the confounding factors of using different model configurations across the myriad of WRF physics options, while alleviating the difficulty in understanding their impacts on air quality predictions. The operational GFSv16 and associated

19

reanalysis products are well vetted and evaluated across different global agencies and laboratories, and thus are well suited for regional CMAQ applications using NACC. In fact, there is an ongoing project at NOAA to migrate both the GFSv16 data and NACC software to the Amazon Web Services (AWS) Cloud platform to provide a streamlined product for the user to generate the model-ready meteorological data for any regional CMAQ application globally.

Finally, we note that the current operational GFSv16 has all needed meteorological variables to drive CMAQ, and users have option to supply other data (fractional landuse, LAI etc). GFSv16's C768 grid has horizontal resolution from 10.21 km to 14.44 km, which is close to the NAQFC's 12 km horizontal resolution. One barrier of using this NACC approach is that the original-resolution GFS data files with all needed variables are very big even with compression (about 8GB per time step), and may not be accessible for community users. There is an ongoing effort of using cloud storages to solve this issue, and making this method available to the community. Traditional WRF-CMAQ usually starts from commonly available global meteorological data, such as NCEP or ECMWF reanalysis data, which are in relatively coarse resolution, and use WRF to generate all meteorological variables needed by CMAQ in native grid. In some cases, the WRF may become the only available method to drive a finer scale CMAQ model application. WRF's various physics can also be customized for CMAQ simulation over certain regions or under certain meteorological conditions. Both methods have its pros and cons. As shown in this study, GFS and WRF had mixed performance for driving CMAQ, though they are overall similar.

Code and Data Availability.

The FIREX-AQ field campaign data used in this study is in https://www-air.larc.nasa.gov/cgi-bin/ArcView/firexaq (last access, 16 May 2022). The NACC code used in this study is publicly available at https://doi.org/10.5281/zenodo.5507489 and via GitHub at https://github.com/noaa-oar-arl/NACC.git (last access: 5 April 2022). The modified CMAQv5.3.1 for GFS-CMAQ is available at https://doi.org/10.5281/zenodo.5507511 and via GitHub at https://github.com/noaa-oar-arl/NAQFC (last access: 5 April 2022).

Author contributions.

YT contributed to the project conceptualization, model run, software, data analysis, visualization, investigation, and writing of the original draft. PCC contributed to software, the model run, data analysis, investigation and draft revision. DT and XZ contributed to wildfire emissions data. BB contributed to software and funding acquisition. FY, JH and HH provided the GFS model data. LP provided the global aerosol model for the lateral boundary condition. PL, RS, AS, JF, IS, JT-D, YJ contributed to project supervision, project administration, and funding acquisition. MY, IB, JF, TR, DB, JS, J-LJ, JC, GD, RM, JH, GH, AR and JD contributed to the FIREX-AQ aircraft data.

20

References:

Appel, K.W., Bash, J.O., Fahey, K.M., Foley, K.M., Gilliam, R.C., Hogrefe, C., Hutzell, W.T., Kang, D., Mathur, R., Murphy, B.N. and Napelenok, S.L.,. The Community Multiscale Air Quality (CMAQ) model versions 5.3 and 5.3. 1: system updates and evaluation. Geoscientific Model Development, 14(5), pp.2867-2897. 2021. https://doi.org/10.5194/gmd-14-2867-2021

Arakawa, A. and Lamb, V.: Computational design of the basic dynamical processes of the UCLA general circulation model, Methods in Computational Physics, 17, 173–265, 1977.

Baker, K.R., Woody, M.C., Tonnesen, G.S., Hutzell, W., Pye, H.O.T., Beaver, M.R., Pouliot, G. and Pierce, T., Contribution of regional-scale fire events to ozone and PM2. 5 air quality estimated by photochemical modeling approaches. Atmospheric Environment, 140, 539-554. https://doi.org/10.1016/j.atmosenv.2016.06.032, 2016.

Briggs, G. A., A Plume Rise Model Compared with Observations, Journal of the Air Pollution Control Association, 15:9, 433-438, doi:10.1080/00022470.1965.10468404, 1965.

Byun, D. W., Dynamically Consistent Formulations in Meteorological and Air Quality Models for Multiscale Atmospheric Studies. Part I: Governing Equations in a Generalized Coordinate System, Journal of the Atmospheric Science, 56, 3789–3807. 1999a. https://doi.org/10.1175/1520-0469(1999)056<3789:DCFIMA>2.0.CO;2

Byun, D.W., Dynamically consistent formulations in meteorological and air quality models for multi-scale atmospheric applications: Part II. Mass conservation issues. Journal of the Atmospheric Science 56, 3808–3820, 1999b. https://doi.org/10.1175/1520-0469(1999)056<3808:DCFIMA>2.0.CO;2.

Byun, D.W., Ching, J.K.S.. Science algorithms of the EPA models-3 Community Multiscale Air Quality (CMAQ) modeling system, EPA/600/R-99/030, U.S. EPA. 1999c

Byun, D. and Schere, K.L.,. Review of the governing equations, computational algorithms, and other components of the Models-3 Community Multiscale Air Quality (CMAQ) modeling system. Appl. Mech. Rev. 59: 51–77. https://doi.org/10.1115/1.2128636. 2006.

Campbell, P., Tang, Y., Lee, P., Baker, B., Tong, D., Saylor, R., Stein, A., Huang, J., Huang, H.-C., Strobach, E., McQueen, J., Pan, L., Stajner, I., Sims, J., Tirado-Delgado, J., Jung, Y., Yang, F., Spero, T., and Gilliam, R.: Development and evaluation of an advanced National

21

Air Quality Forecast Capability using the NOAA Global Forecast System version 16, Geosci. Model Dev. 15, 3281–3313, https://doi.org/10.5194/gmd-15-3281-2022, 2022.

Chen, F., and Dudhia, J. Coupling an advanced land surface-hydrology model with the Penn State-NCAR MM5 modeling system. Part I: Model implementation and sensitivity. Monthly Weather Review, 129(4), 569–585. 2001. https://doi.org/10.1175/1520-0493(2001)129<0569:CAALSH>2.0.CO;2

Chen J.-H and S.-J Lin. The remarkable predictability of inter-annual variability of atlantic hurricanes during the past decade. Geophysical Research Letters, 38(L11804):6, 2011. https://doi.org/10.1029/2011GL047629

Chen J-H.and S-J. Lin. Seasonal predictions of tropical cyclones using a 25-km-resolution general circulation model. J. Climate, 26(2):380–398, 2013. https://doi.org/10.1175/JCLI-D-12-00061.1

Clough, S. A., Shephard, M. W., Mlawer, J. E., Delamere, J. S., Iacono, M. J., Cady-Pereira, K., et al. (2005). Atmospheric radiative transfer modeling: A summary of the AER codes. Journal of Quantitative Spectroscopy & Radiative Transfer, 91(2), 233–244. https://doi.org/10.1016/j.jqsrt.2004.05.058

Caputi, D. J., Faloona, I., Trousdell, J., Smoot, J., Falk, N., and Conley, S.: Residual layer ozone, mixing, and the nocturnal jet in California's San Joaquin Valley, Atmos. Chem. Phys., 19, 4721–4740, https://doi.org/10.5194/acp-19-4721-2019, 2019

Dong, X., J. S. Fu, K. Huang, D. Tong, and G. Zhuang. Model development of dust emission and heterogeneous chemistry within the Community Multiscale Air Quality modeling system and its application over East Asia. Atmos. Chem. Phys., 16, 8157-8180. 2016. https://doi.org/10.5194/acp-16-8157-2016.

Ek, M. B., Mitchell, K. E., Lin, Y., Rogers, E., Grunmann, P., Koren, V., et al. (2003). Implementation of Noah land surface model advances in the National Centers for Environmental Prediction operational mesoscale Eta model. Journal of Geophysical Research, 108(D22), 8851. https://doi.org/10.1029/2002JD003296

Fischer, E. V., Jacob, D. J., Yantosca, R. M., Sulprizio, M. P., Millet, D. B., Mao, J., Paulot, F., Singh, H. B., Roiger, A., Ries, L., Talbot, R. W., Dzepina, K., and Pandey Deolal, S.: Atmospheric peroxyacetyl nitrate (PAN): a global budget and source attribution, Atmos. Chem. Phys., 14, 2679–2698, https://doi.org/10.5194/acp-14-2679-2014, 2014.

Fu, X., S. X. Wang, Z. Cheng, J. Xing, B. Zhao, J. D. Wang, and J. M. Hao, 2014: Source, transport and impacts of a heavy dust event in the Yangtze River Delta, China, in 2011. Atmos. Chem. Phys., 14, 1239–1254, doi:10.5194/acp-14-1239-2014.

Grell, G. A., Dudhia, J., and Stauffer, D. R. A description of the fifth-generation Penn State/NCAR Mesoscale Model (MM5). NCAR tech. Note NCAR TN-398-1-STR, 117 pp. 1994.

Han, J., & Bretherton, C. S., TKE-Based Moist Eddy-Diffusivity Mass-Flux (EDMF) Parameterization for Vertical Turbulent Mixing, Weather and Forecasting, 34(4), 869-886. 2019. https://doi.org/10.1175/WAF-D-18-0146.1

Harris, L., Chen, X., Putman, W., Zhou, L. and Chen, J.H., A Scientific Description of the GFDL Finite-Volume Cubed-Sphere Dynamical Core. https://doi.org/10.25923/6nhs-5897. 2021

Hodyss, D. and N. Nichols, The error of representation: basic understanding, Tellus A: Dynamic Meteorology and Oceanography, 67:1, https://doi.org/10.3402/tellusa.v67.24822, 2015.

Hong, Song–You, Yign Noh, Jimy Dudhia, A new vertical diffusion package with an explicit treatment of entrainment processes. Mon. Wea. Rev., 134, 2318–2341. 2006. doi:10.1175/MWR3199.1.

Houyoux, M.R., Vukovich, J.M., Coats, C.J., Wheeler, N.J.M., Kasibhatla, P.S.,. Emission inventory development and processing for the seasonal model for regional air quality (SMRAQ) project. J. Geophys. Res., 105(D7), 9079-9090, https://doi.org/10.1029/1999JD900975. 2000.

Huang, M., D. Tong, P. Lee, L. Pan, Y. Tang, I. Stajner, R. B. Pierce, J. McQueen, and J. Wang, Toward enhanced capability for detecting and predicting dust events in the western United States: The Arizona case study. Atmos. Chem. Phys., 15, 12 595–12 610, doi:10.5194/acp-15-12595-2015. 2015.

Kain, J. S., The Kain–Fritsch convective parameterization: An update. J. Appl. Meteor., 43, 170–181. doi:10.1175/1520-0450(2004)043<0170:TKCPAU>2.0.CO;2, 2004.

Kim, Y.J., Eckermann, S.D. and Chun, H.Y., An overview of the past, present and future of gravity-wave drag parameterization for numerical climate and weather prediction models. Atmosphere-Ocean, 41(1), 65-98., doi: 10.3137/ao.410105, 2003.

Krueger, S. K., Q. Fu, K. N. Liou, and H-N. S. Chin. Improvement of an ice-phase microphysics parameterization for use in numerical simulations of tropical convection. Journal of Applied Meteorology, 34:281–287, January 1995. https://doi.org/10.1175/1520-0450-34.1.281

Iacono, M. J., Delamere, J. S., Mlawer, E. J., Shephard, M. W., Clough, S. A., and Collins, W. D.. Radiative forcing by long-lived greenhouse gases: Calculations with the AER radiative transfer models. Journal of Geophysical Research, 113, D13103. 2008. https://doi.org/10.1029/2008JD009944

Jimenez, P. A., Dudhia, J., Gonzalez-Rouco, J. F., Navarro, J., Montavez, J. P., & Garcia-Bustamante, E. (2012). A revised scheme for the WRF surface layer formulation. Monthly Weather Review, 140(3), 898–918. https://doi.org/10.1175/MWR-D-11-00056.1

Lin, Y.-L., R. D. Farley, and H. D. Orville. Bulk parameterization of the snow field in a cloud model. J. Climate Appl. Meteor., 22:1065–1092, 1983. https://doi.org/10.1175/1520-0450(1983)022<1065:BPOTSF>2.0.CO;2

Lord, S. J., H.E. Willoughby, and J.M. Piotrowicz. Role of a parameterized ice-phase microphysics in an axisymmetric, nonhydrostatic tropical cyclone model. J. Atmos. Sci., 41(19):2836–2848, October 1984. https://doi.org/10.1175/1520-0469(1984)041<2836:ROAPIP>2.0.CO;2

Lu, Q., Murphy, B. N., Qin, M., Adams, P. J., Zhao, Y., Pye, H. O. T., Efstathiou, C., Allen, C., and Robinson, A. L.: Simulation of organic aerosol formation during the CalNex study: updated mobile emissions and secondary organic aerosol parameterization for intermediate-

23

volatility organic compounds, Atmos. Chem. Phys., 20, 4313–4332, https://doi.org/10.5194/acp-20-4313-2020, 2020

Luecken, D. J., Yarwood, G., and Hutzell, W. T.: Multipollutant modeling of ozone, reactive nitrogen and HAPs across the continental US with CMAQ-CB6, Atmos. Environ., 201, 62–72, https://doi.org/10.1016/j.atmosenv.2018.11.060 , 2019.

Mlawer, E. J., Taubman S. J., Brown P. D., Iacono M. J., and Clough S. A., Radiative transfer for inhomogeneous atmospheres: RRTM, a validated correlated-k model for the longwave. J. Geophys. Res., 102, 16663–16682. 1997. https://doi.org/10.1029/97JD00237.

Monin, A. S., & Obukhov, A. M. Basic laws of turbulent mixing in the surface layer of the atmosphere (in Russian). Contribution Geophysics Institute, Academy of Sciences USSR, 151, 163–187. 1954.

Morrison, H., G. Thompson, V. Tatarskii, 2009: Impact of Cloud Microphysics on the Development of Trailing Stratiform Precipitation in a Simulated Squall Line: Comparison of One– and Two–Moment Schemes. Mon. Wea. Rev., 137, 991–1007. https://doi.org/10.1175/2008MWR2556.1

National Emissions Inventory Collaborative (2019). 2016v1 Emissions Modeling Platform. Retrieved from http://views.cira.colostate.edu/wiki/wiki/10202.

Ott, E., Hunt, B.R., Szunyogh, I., Zimin, A.V., Kostelich, E.J., Corazza, M., Kalnay, E., Patil, D.J. and Yorke, J.A., 2004. A local ensemble Kalman filter for atmospheric data assimilation. *Tellus A: Dynamic Meteorology and Oceanography*, *56*(5), pp.415-428. https://doi.org/10.3402/tellusa.v56i5.14462

Otte, T. L., J E. Pleim, and G Pouliot. PREMAQ: A new pre-processor to cmaq for air-quality forecasting. Presented at 2004 Models-3 Conference, Chapel Hill, NC, October 18-20, 2004.

Otte, T. L. and Pleim, J. E.: The Meteorology-Chemistry Interface Processor (MCIP) for the CMAQ modeling system: updates through MCIPv3.4.1, Geosci. Model Dev., 3, 243–256, https://doi.org/10.5194/gmd-3-243-2010, 2010.

Pan, L., Kim, H., Lee, P., Saylor, R., Tang, Y., Tong, D., Baker, B., Kondragunta, S., Xu, C., Ruminski, M. G., Chen, W., McQueen, J., and Stajner, I.: Evaluating a fire smoke simulation algorithm in the National Air Quality Forecast Capability (NAQFC) by using multiple observation data sets during the Southeast Nexus (SENEX) field campaign, Geosci. Model Dev., 13, 2169–2184, https://doi.org/10.5194/gmd-13-2169-2020 , 2020.

Parrish, D. D., Ryerson, T. B., Mellqvist, J., Johansson, J., Fried, A., Richter, D., Walega, J. G., Washenfelder, R. A., de Gouw, J. A., Peischl, J., Aikin, K. C., McKeen, S. A., Frost, G. J., Fehsenfeld, F. C., and Herndon, S. C.: Primary and secondary sources of formaldehyde in urban atmospheres: Houston Texas region, Atmos. Chem. Phys., 12, 3273–3288, https://doi.org/10.5194/acp-12-3273-2012, 2012.

Peterson, D.A., Fromm, M.D., McRae, R.H., Campbell, J.R., Hyer, E.J., Taha, G., Camacho, C.P., Kablick, G.P., Schmidt, C.C. and DeLand, M.T., Australia's Black Summer pyrocumulonimbus super outbreak reveals potential for increasingly extreme stratospheric

smoke events. npj Climate and Atmospheric Science, 4(1), 2021.
https://doi.org/10.1038/s41612-021-00192-9

Poggio, L., de Sousa, L. M., Batjes, N. H., Heuvelink, G. B. M., Kempen, B., Ribeiro, E., and
Rossiter, D.: SoilGrids 2.0: producing soil information for the globe with quantified spatial
uncertainty, SOIL, 7, 217–240, 2021. https://doi.org/10.5194/soil-7-217-2021

Powers, J.G., Klemp, J.B., Skamarock, W.C., Davis, C.A., Dudhia, J., Gill, D.O., Coen, J.L.,
Gochis, D.J., Ahmadov, R., Peckham, S.E. and Grell, G.A.,. The weather research and
forecasting model: Overview, system efforts, and future directions. Bulletin of the American
Meteorological Society, 98(8), pp.1717-1737. 2017. https://doi.org/10.1175/BAMS-D-15-
00308.1

Putman, W. M. and S.-J. Lin, Finite-volume transport on various cubed-sphere grids, Journal of
Computational Physics, 227(1), 55-78, https://doi.org/10.1016/j.jcp.2007.07.022, 2007.

Qian, Y., Yang, Z., Feng, Z., Liu, Y., Gustafson, W.I., Berg, L.K., Huang, M., Yang, B. and Ma,
H.Y., Neglecting irrigation contributes to the simulated summertime warm-and-dry bias in the
central United States. npj Clim Atmos Sci 3, 31. https://doi.org/10.1038/s41612-020-00135-
w, 2020

Rolph, G. D., Draxler, R. R., Stein, A. F., Taylor, A., Ruminski, M. G., Kondragunta, S., Zeng,
J., Huang, H. C., Manikin, G., McQueen, J. T., and Davidson, P. M.: Description and
Verification of the NOAA Smoke Forecasting System: The 2007 Fire Season, Weather
Forecast., 24, 361–378. https://doi.org/10.1175/2008waf2222165.1, 2009.

Skamarock, W. C., Klemp, J. B., Dudhia, J., Gill, D. O., Liu, Z., Berner, J., Huang, X.-Yu.. A
Description of the Advanced Research WRF Model Version 4. NCAR Tech Note,
NCAR/TN–556+STR. doi:10.5065/1dfh-6p97, 2021.

Skamarock, W.C., Snyder, C., Klemp, J.B. and Park, S.H., vertical resolution requirements in
atmospheric simulation. Monthly Weather Review, 147(7), 2641-2656.
https://doi.org/10.1175/MWR-D-19-0043.1, 2019.

Shi, Y., Hu, F., Xiao, Z., Fan, G. and Zhang, Z., Comparison of four different types of planetary
boundary layer heights during a haze episode in Beijing. Science of the total environment,
711, https://doi.org/10.1016/j.scitotenv.2019.134928, 2020.

Sillman, S., He, D., Cardelino, C., and Imhoff, R. E.: The use of photochemical indicators to
evaluate ozone-NOx –hydrocarbon sensitivity: Case studies from Atlanta, New York, and Los
Angeles, J. Air Waste Manage. Assoc., 47, 1030–1040,
doi:10.1080/10962247.1997.11877500, 1997.

Sofiev, M., Ermakova, T., and Vankevich, R.: Evaluation of the smoke-injection height from
wild-land fires using remote-sensing data, Atmos. Chem. Phys., 12, 1995–2006,
https://doi.org/10.5194/acp-12-1995-2012, 2012.

Tewari, M., Chen, F., Wang, W., Dudhia, J., LeMone, M. A., Mitchell, K., et al. Implementation
and verification of the unified NOAH land surface model in the WRF model. Paper Presented
at the 20th Conference on Weather Analysis and Forecasting/16th Conference on Numerical
Weather Prediction, Seattle, WA, 2004.

25

Wang, S., Coggon, M.M., Gkatzelis, G.I., Warneke, C., Bourgeois, I., Ryerson, T., Peischl, J., Veres, P.R., Neuman, J.A., Hair, J. and Shingler, T,. Chemical Tomography in a Fresh Wildland Fire Plume: a Large Eddy Simulation (LES) Study. Journal of Geophysical Research: Atmospheres, 126(18), https://doi.org/10.1029/2021JD035203. 2021

Wiedinmyer, C., Akagi, S.K., Yokelson, R.J., Emmons, L.K., Al-Saadi, J.A., Orlando, J.J. and Soja, A.J., 2011. The Fire INventory from NCAR (FINN): A high resolution global model to estimate the emissions from open burning. Geoscientific Model Development, 4(3), pp.625-641. doi:10.5194/gmd-4-625-2011.

Yamartino, R. J., Nonnegative, conserved scalar transport using grid-cell-centered, spectrally constrained Blackman cubics for applications on a variable-thickness mesh. Mon. Wea. Rev. 121, 753-763, 1999. https://doi.org/10.1175/1520-493(1993)121<0753:NCSTUG>2.0.CO;2

Yang, F., Tallapragada, V., Kain, J. S., Wei, H., Yang, R., Yudin, V. A., Moorthi, S., Han, J., Hou, Y. T., Wang, J., Treadon, R., and Kleist, D. T. (2020). Model Upgrade Plan and Initial Results from a Prototype NCEP Global Forecast System Version 16. 2020 AMS Conference, Boston, MA. https://ams.confex.com/ams/2020Annual/webprogram/Paper362797.html

Yarwood, G., Jung, J., Whitten, G.Z., Heo, G., Mellberg, J. and Estes, M., Updates to the Carbon Bond mechanism for version 6 (CB6). In 9th Annual CMAS Conference, Chapel Hill, NC (pp. 11-13). 2010.

Yarwood, Y., Sakulyanontvittaya, T., Nopmongcol, O., and Koo, K.: Ozone depletion by bromine and iodine over the Gulf of Mexico, final report for the Texas Commission on Environmental Quality, available at: https://www.tceq.texas.gov/assets/public/implementation/air/am/contracts/reports/pm/5821110365FY1412-20141109-environ-bromine.pdf (last access: 3 May 2021), November 2014.

Ye, X., Arab, P., Ahmadov, R., James, E., Grell, G. A., Pierce, B., Kumar, A., Makar, P., Chen, J., Davignon, D., Carmichael, G. R., Ferrada, G., McQueen, J., Huang, J., Kumar, R., Emmons, L., Herron-Thorpe, F. L., Parrington, M., Engelen, R., Peuch, V.-H., da Silva, A., Soja, A., Gargulinski, E., Wiggins, E., Hair, J. W., Fenn, M., Shingler, T., Kondragunta, S., Lyapustin, A., Wang, Y., Holben, B., Giles, D. M., and Saide, P. E.: Evaluation and intercomparison of wildfire smoke forecasts from multiple modeling systems for the 2019 Williams Flats fire, Atmos. Chem. Phys., 21, 14427–14469, https://doi.org/10.5194/acp-21-14427-2021, 2021.

Yu, S., Mathur, R., Pleim, J., Pouliot, G., Wong, D., Eder, B., Schere, K., Gilliam, R. and Rao, S.T. Comparative evaluation of the impact of WRF/NMM and WRF/ARW meteorology on CMAQ simulations for PM2.5 and its related precursors during the 2006 TexAQS/GoMACCS study. Atmospheric Chemistry and Physics, 12(9), doi:10.5194/acp-12-4091-2012, 2012a.

Yu, S., Mathur, R., Pleim, J., Pouliot, G., Wong, D., Eder, B., Schere, K., Gilliam, R. and Rao, S.T., 2012. Comparative evaluation of the impact of WRF–NMM and WRF–ARW meteorology on CMAQ simulations for O3 and related species during the 2006

TexAQS/GoMACCS campaign. Atmospheric Pollution Research, 3(2), pp.149-162, doi: 10.5094/APR.2012.015, 2012b.

Zhang, X., and Kondragunta, S., 2006, Estimating forest biomass in the USA using generalized allometric model and MODIS land data, Geographical Research Letter, 33, L09402, doi:10.1029/2006GL025879.

Zhang, X., Kondragunta, S., and Quayle, B. Estimation of biomass burned areas using multiple-satellite-observed active fires. IEEE Transactions on Geosciences and Remote Sensing, 49: 4469-4482, 10.1109/TGRS.2011.2149535, 2011.

Zhuang, J., Jacob, D. J., and Eastham, S. D.: The importance of vertical resolution in the free troposphere for modeling intercontinental plumes, Atmos. Chem. Phys., 18, 6039–6055, https://doi.org/10.5194/acp-18-6039-2018, 2018.

27

1   Table 1. The two meteorological datasets used in this study

| Model Settings	FV3-GFSv16/NACC	WRF-ARW/MCIP
Domain	Global C768L127 (~ 13 km horizontal resolution in 6 cubic spherical tiles , 127 vertical layers up to 80km), interpolated to the 12km CONUS domain with 35-layers up to about 14km (60hPa)	12km CONUS 35 vertical layers up to 100hPa
Dynamic core	Finite Volume 3, non-hydrostatic (Putman and Lin, 2007)	WRF-ARW dynamic in hybrid vertical coordinate (Skamarock et al., 2021)
Initial condition	FV3-GFSv16 analysis (GDAS) using the local ensemble Kalman filter (LETKF) (Ott et al., 2004) with 4-dimensional incremental analysis update (4D-IAU)	FV3-GFSv16 analysis (GDAS)
Lateral Boundary Condition	N/A	FV3-GFSv16 analysis (GDAS)
Cloud Microphysics	GFDL six-category cloud microphysics scheme (Lin et al., 1983; Lord et al., 1984; Krueger et al., 1995; Chen and Lin, 2011; Chen and Lin, 2013)	Morrison 2-moment scheme (Morrison et al., 2009)
PBL Physics Scheme	Scale-aware (sa) turbulent kinetic energy (TKE) -based moist eddy-diffusivity mass-flux (EDMF) (sa-TKE-EDMF) (Han and Bretherton,2019)	Yonsei University Scheme (Hong et al., 2006)
Shallow/Deep Cumulus Parameterization	SAS Scheme (Han et al. 2011; 2017)	Kain Fritsch multiscale (Kain, 2004)
Shortwave and Longwave Radiation	RRTMG (Mlawer et al. 1997; Clough et al. 2005; Iacono et al. 2008)	RRTMG (Iacono et al. 2008).
Land Surface Model	Noah Land Surface Model (Chen and Dudhia 2001; Ek et al. 2003;Tewari et al. 2004)	Noah (Tewari et al., 2004)
Surface Layer	Monin-Obukhov (Monin-Obukhov 1954; Grell et al. 1994; Jimenez et al. 2012)	Revised MM5 Scheme (Jimenez et al., 2012)
Other treatment		FDDA nudging is enabled for temperature and specific humidity whole domain, and for wind components (U, V) outside the PBL.

2

28

Variables	Obs Mean	GFS-CMAQ					WRF-CMAQ				
		MB	NMB	RMSE	R	Slope	MB	NMB	RMSE	R	Slope
Temperature (K)	295	0.979	0.332	2.04	0.988	1.13	1.16	0.393	2.28	0.989	1.17
RH (%)	35.6	-7.3	-20.5	11.8	0.781	0.717	-6.05	-17	12.6	0.677	0.598
Wind Speed (m/s)	4.81	0.758	15.8	3.25	0.432	0.473	-1.11	-23.1	2.4	0.666	0.524
O_3 (ppbv)	57.9	-10.7	-18.5	15	0.651	0.34	-10.4	-17.9	14.1	0.717	0.413
CO (ppbv)	134	-37.6	-28	53.2	0.654	0.573	-37.1	-27.7	52.9	0.652	0.572
NOx (ppbv)	1.11	0.507	45.6	2.9	0.704	1.15	0.345	31.1	2.86	0.695	1.12
NOy (ppbv)	2.56	-0.0418	-1.63	3.07	0.743	0.892	0.055	2.15	3.14	0.724	0.86
NOz (ppbv)	1.63	-0.465	-28.6	1.17	0.782	0.553	-0.125	-7.66	1.08	0.788	0.721
HONO (ppbv)	0.00432	0.012	279	0.0438	0.379	0.444	0.0134	311	0.0487	0.358	0.48
HNO_3 (ppbv)	0.291	0.154	53.1	0.421	0.683	1.34	0.337	116	0.65	0.708	1.89
PAN (ppbv)	0.399	-0.251	-63	0.416	0.675	0.221	-0.222	-55.6	0.386	0.681	0.284
NH_3 (ppbv)	3.55	-0.801	-22.6	5.26	0.0481	0.038	-1.58	-44.5	4.37	0.304	0.155
C_2H_4 (ppbv)	0.121	0.0582	48.1	0.189	0.702	0.869	0.0385	31.9	0.187	0.682	0.836
C_2H_2 (ppbv)	0.146	-0.0734	-50.3	0.137	0.784	0.496	-0.0696	-47.7	0.137	0.771	0.494
SO_2 (ppbv)	0.342	-0.235	-68.8	0.567	0.0238	0.00835	-0.221	-64.5	0.568	-1.26×10^{-3}	-0.00047
Acetone (ppbv)	2.74	-2.28	-83.1	2.45	0.686	0.192	-2.2	-80.4	2.38	0.668	0.199
HCHO (ppbv)	2.1	-0.972	-46.4	1.26	0.559	0.447	-0.909	-43.4	1.25	0.513	0.442
CH_3CHO (ppbv)	0.736	-0.326	-44.2	0.538	0.647	0.386	-0.349	-47.4	0.554	0.643	0.38
Benzene (ppbv)	0.0449	-0.0193	-43	0.057	0.398	0.385	-0.0191	-42.6	0.0564	0.397	0.375
Toluene (ppbv)	0.039	0.0409	105	0.153	0.759	1.74	0.0352	90.1	0.14	0.762	1.63
Isoprene (ppbv)	0.073	0.0361	49.4	0.174	0.6	0.838	0.00661	9.06	0.145	0.648	0.797
EC (μg/std m^3)	0.108	0.191	177	0.572	0.518	2.09	0.228	211	0.609	0.455	1.88
OA (μg/std m^3)	10.9	-7.15	-65.7	9.72	0.565	0.263	-6.48	-59.5	9.45	0.495	0.243
Sulfate (μg/std m^3)	1.31	-0.781	-59.7	1.11	0.0856	0.0188	-0.773	-59	1.11	0.0322	0.00677
NH_4^+ (μg/std m^3)	0.745	-0.615	-82.5	0.805	0.416	0.103	-0.596	-79.9	0.778	0.509	0.145
Nitrate (μg/std m^3)	1.22	-1.08	-88.1	1.49	0.562	0.229	-1.04	-85.3	1.45	0.57	0.279
AOE (/Mm)	54.5	-29.3	-53.8	47	0.593	0.227	-27.4	-50.2	45.9	0.588	0.227

Table 2. Statistics of the two models compared to the observation for DC-8 flight segments without fire influences below 3km (ASL) over west of -100°W. All aerosols are in submicron. The normalized mean bias (NMB) is in unit %.

Variables	Obs Mean	GFS-CMAQ					WRF-CMAQ				
		MB	NMB	RMSE	R	Slope	MB	NMB	RMSE	R	Slope
Temperature (K)	287	-0.389	-0.135	0.702	0.995	1.01	-0.688	-0.24	0.863	0.997	1.04
RH (%)	27.8	-0.761	-2.74	7.84	0.712	0.553	4.3	15.5	11.1	0.556	0.534
Wind Speed (m/s)	5.42	0.766	14.1	2.16	0.612	0.616	-0.811	-15	2.12	0.604	0.556
O_3 (ppbv)	55.7	-6.61	-11.9	11.8	0.587	0.262	-7.01	-12.6	11.5	0.653	0.346
CO (ppbv)	486	-377	-77.6	873	0.596	0.0347	-383	-78.8	883	0.442	0.0242
NOx (ppbv)	2.63	0.06	2.28	6.41	0.465	0.231	-0.619	-23.5	7.02	0.31	0.153
NOy (ppbv)	7.32	-4.19	-57.3	13.3	0.507	0.123	-4.66	-63.7	14.2	0.31	0.073
NOz (ppbv)	5.7	-4.8	-84.3	10.2	-0.189	-0.0106	-4.68	-82	10.2	-0.204	-0.0121
HONO (ppbv)	0.283	-0.274	-96.8	1.18	0.355	0.0043	-0.274	-96.8	1.18	0.291	0.00457
HNO_3 (ppbv)	0.148	0.148	99.7	0.256	0.532	1.07	0.179	121	0.28	0.402	0.768
PAN (ppbv)	0.971	-0.793	-81.7	1.63	0.27	0.0195	-0.765	-78.8	1.61	0.279	0.026
NH_3 (ppbv)	17.7	-12.3	-69.3	28.3	0.379	0.0654	-13.7	-77.4	29.6	0.232	0.0386
C_2H_4 (ppbv)	4.5	-4.34	-96.3	10.2	0.421	0.00498	-4.36	-96.8	10.2	0.14	0.0018
C_2H_2 (ppbv)	1.04	-1.01	-96.9	2.08	0.534	0.00866	-1.01	-97	2.09	0.363	0.00623
SO_2 (ppbv)	0.699	-0.322	-46.1	1.38	0.589	0.198	-0.392	-56.1	1.5	0.429	0.132
Acetone (ppbv)	3.54	-3.2	-90.3	4.56	0.13	0.00862	-3.18	-89.7	4.55	0.135	0.0112
HCHO (ppbv)	8.17	-7.13	-87.3	17.8	0.232	0.0062	-7.19	-88	17.8	0.119	0.00303
CH_3CHO (ppbv)	3.65	-3.18	-87.4	9.13	0.186	0.00547	-3.21	-88	9.2	-0.027	-0.00097
Benzene (ppbv)	0.683	-0.67	-98.1	1.84	0.54	0.00432	-0.672	-98.3	1.84	0.367	0.00275
Toluene (ppbv)	0.451	-0.436	-96.6	1.36	0.402	0.00491	-0.438	-97	1.36	0.195	0.00245
Isoprene (ppbv)	0.095	-7.9×10^{-3}	-8.29	0.234	0.123	0.0579	-0.033	-34.7	0.242	-0.014	-0.00541
EC (μg/std m^3)	1.89	-0.53	-28	3.28	0.612	0.295	-0.787	-41.6	3.7	0.448	0.195
OA (μg/std m^3)	156	-146	-93.4	420	0.612	0.0174	-147	-94.2	423	0.472	0.0122
Sulfate (μg/std m^3)	0.791	-0.116	-14.7	0.676	0.415	0.184	-0.214	-27.1	0.728	0.322	0.13
NH_4^+ (μg/std m^3)	1	-0.591	-59.1	0.931	0.767	0.351	-0.615	-61.5	0.956	0.729	0.359
Nitrate (μg/std m^3)	1.7	-0.56	-32.9	1.47	0.805	0.613	-0.634	-37.2	1.59	0.774	0.599
AOE (/Mm)	391	-350	-89.3	994	0.688	0.027	-357	-91.1	1010.	0.532	0.0152

Table 3, same as Table 2 except for the wildfire affected flight segments.

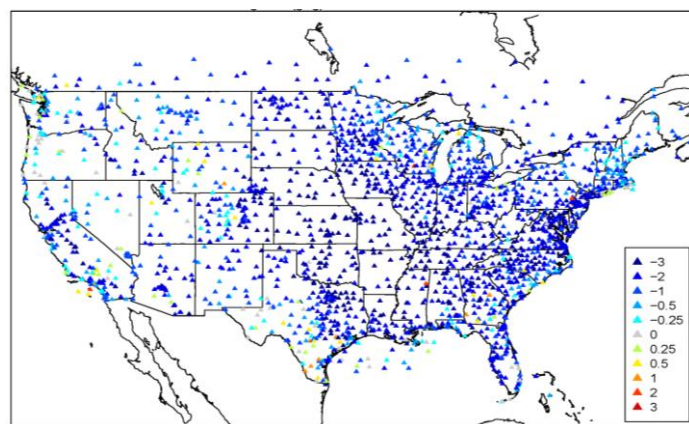a) GFS mean 2m temperature bias (K), 08/2019
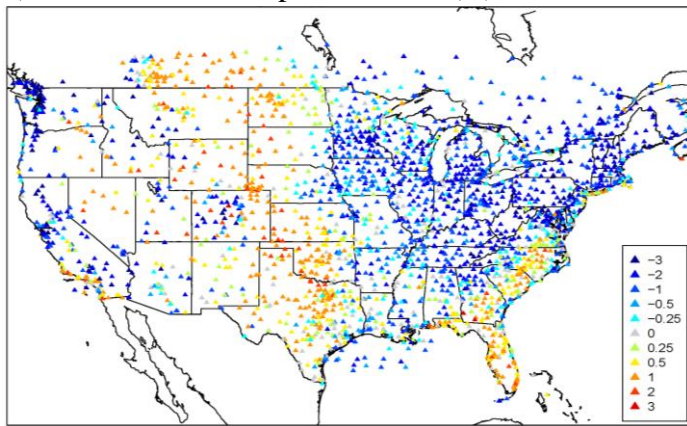
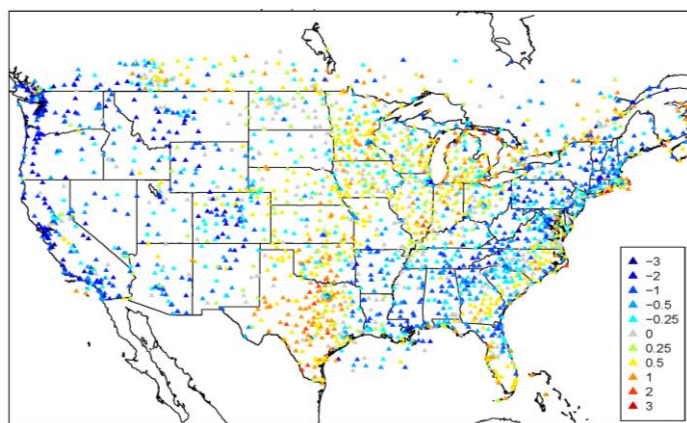b) WRF mean 2m temperature bias (K), 08/2019
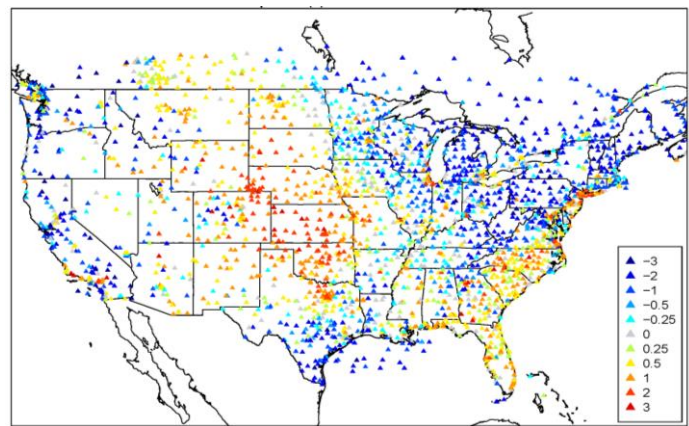
c) GFS mean 2m specific humidity bias (g/kg), 08/2019
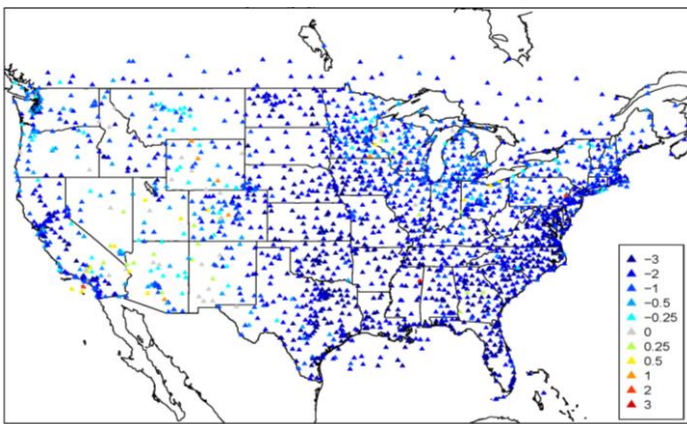
d) WRF mean 2m specific humidity bias (g/kg), 08/2019

e) GFS mean 10m wind speed bias (m/s), 08/2019

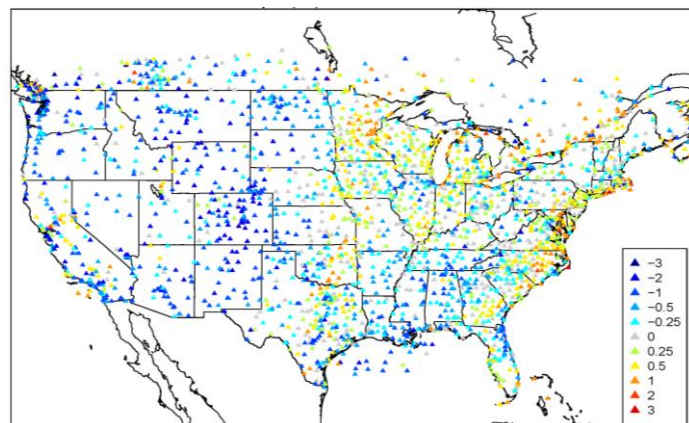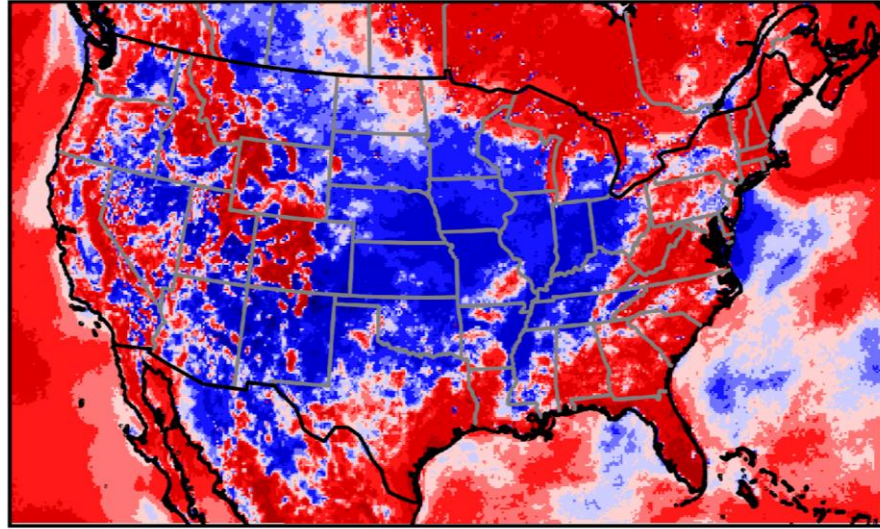f) WRF mean 10m wind speed bias (m/s), 08/2019

Figure 1. GFS and WRF surface meteorological biases for METAR (METeorological Aerodrome Report) stations averaged over August, 2019

a) Monthly Mean PBL Difference (GFS-WRF) at 18UTC

b) Monthly Mean PBL Difference (GFS-WRF) at 06UTC
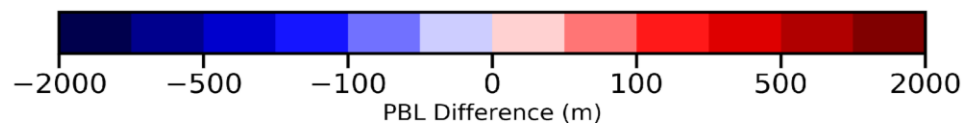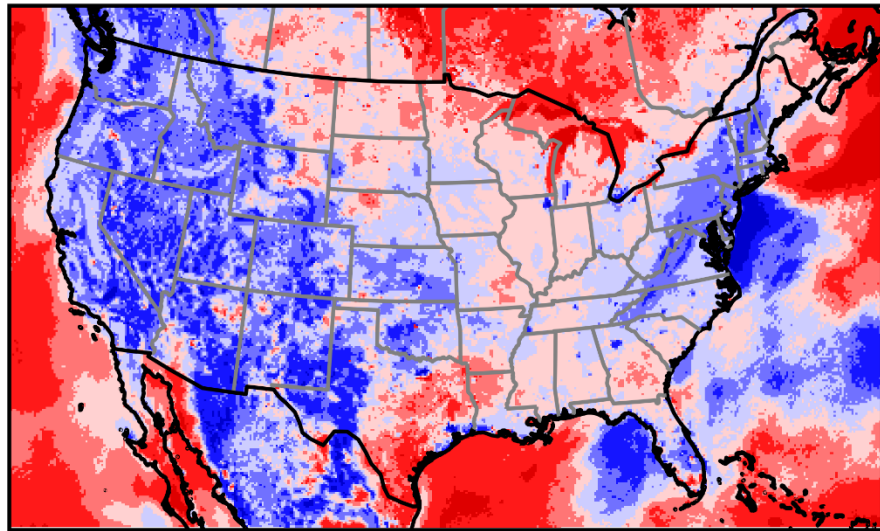
Figure 2. Monthly mean PBL height difference (GFS-WRF) for daytime (a) and nighttime (b), August, 2019.
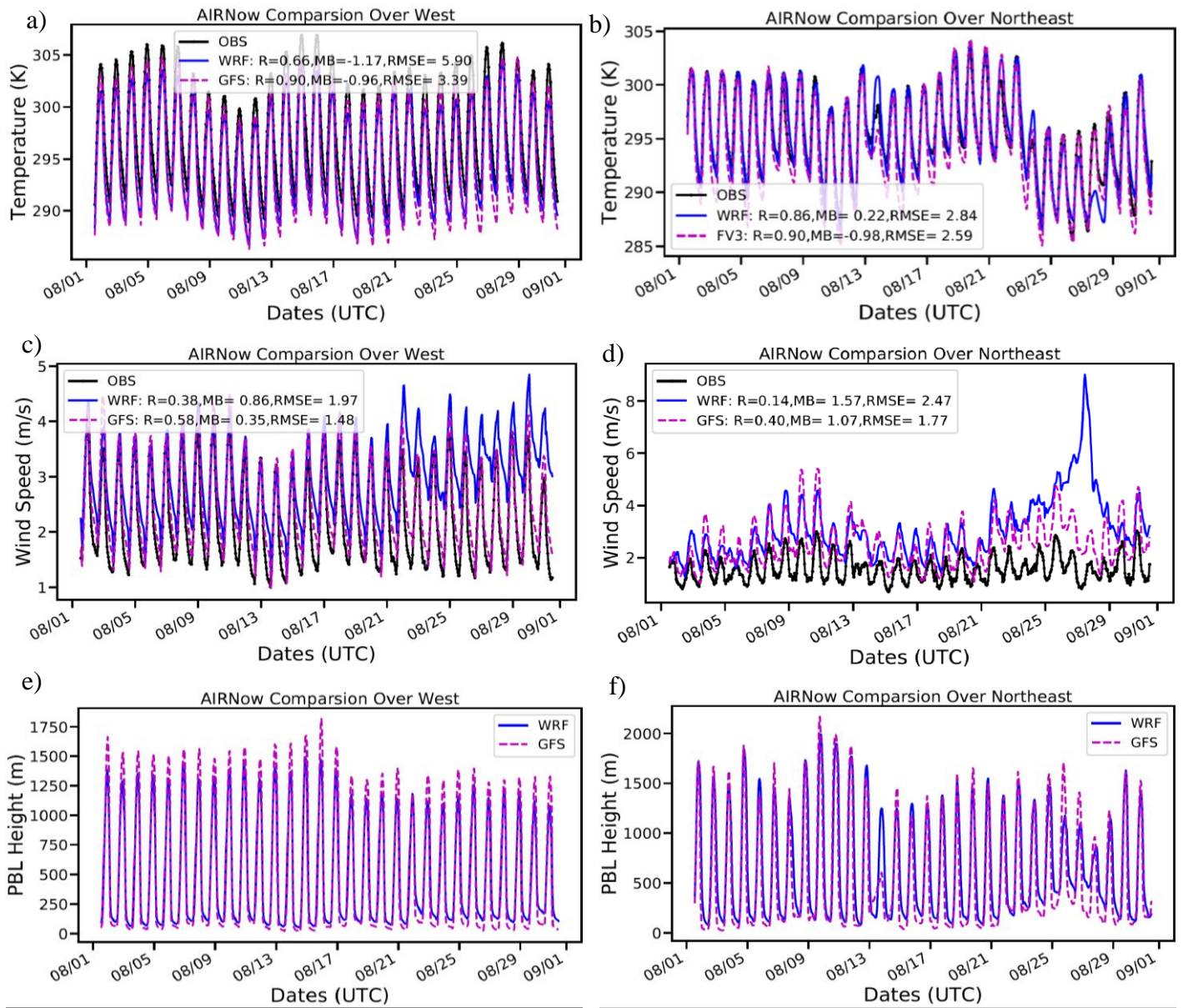
Figure 3. The WRF and GFS time-series comparison over AIRNow stations over the U.S. West and Northeast for 2m temperature (a, b), 10m wind speed (c, d), and PBL height (e,f).

33

a) AIRNow Comparsion Over West

b) AIRNow Comparsion Over Northeast

c) AIRNow Comparsion Over West

d) AIRNow Comparsion Over Northeast
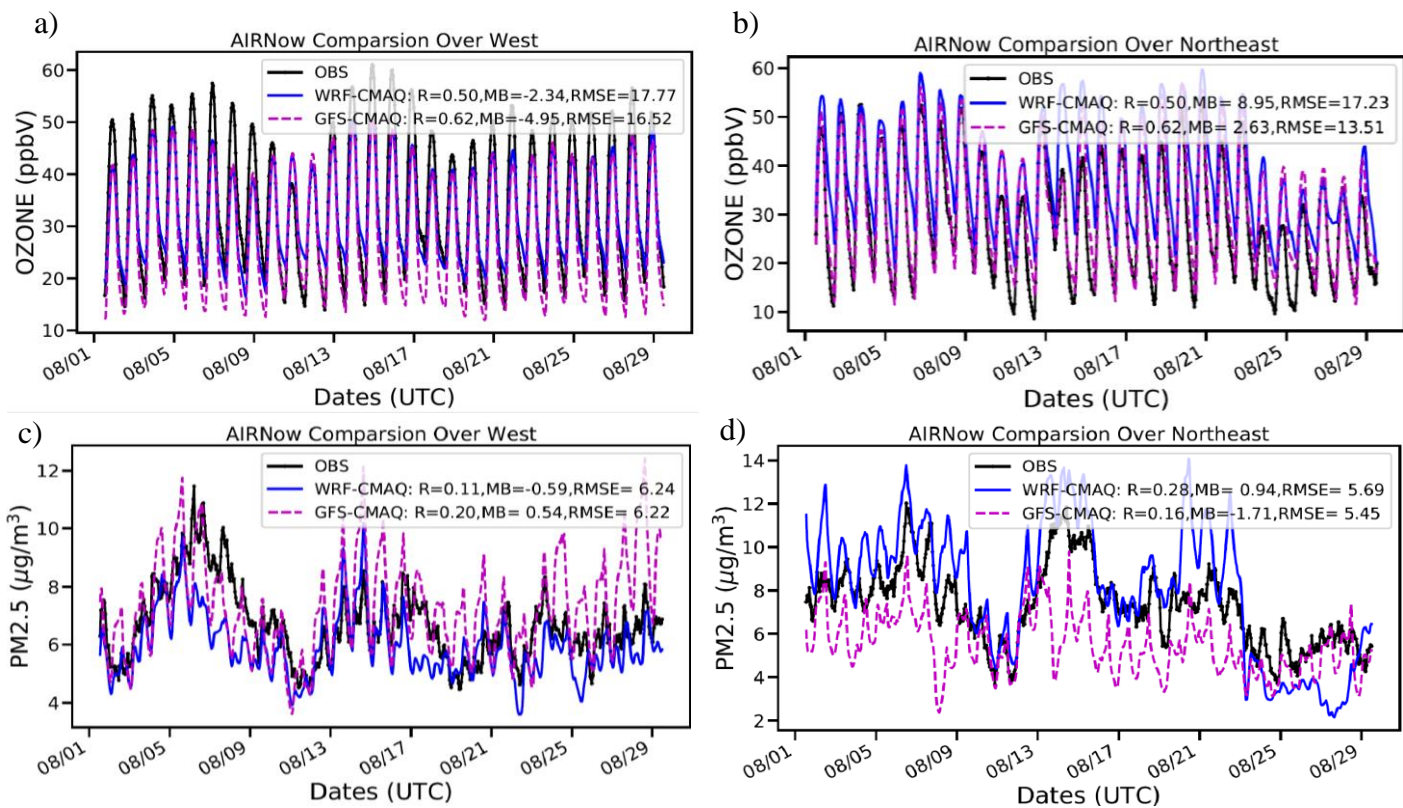
Figure 4. Same as Figure 3 but for ozone (a, b) and PM2.5 (c, d).
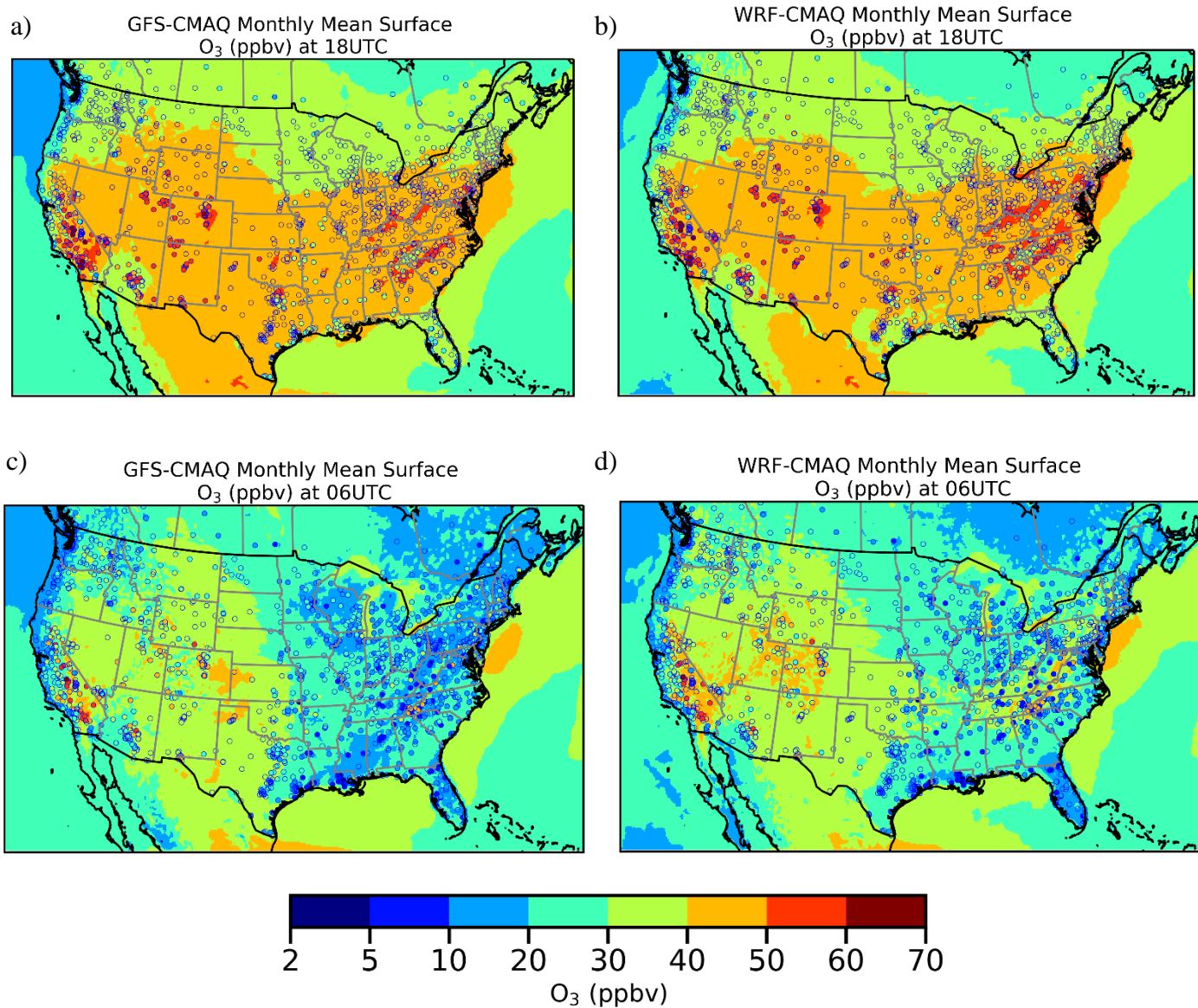
Figure 5. Monthly mean surface ozone predictions by GFS-CMAQ (left plots) and WRF-CMAQ (right plots) for daytime (top plots) and nighttime (bottom plots) compared to the corresponding AIRNow observations, August, 2019

a) GFS-CMAQ Monthly Mean Surface PM2.5 ($\mu g/m^3$) at 18UTC

b) WRF-CMAQ Monthly Mean Surface PM2.5 ($\mu g/m^3$) at 18UTC

c) GFS-CMAQ Monthly Mean Surface PM2.5 ($\mu g/m^3$) at 06UTC

d) WRF-CMAQ Monthly Mean Surface PM2.5 ($\mu g/m^3$) at 06UTC
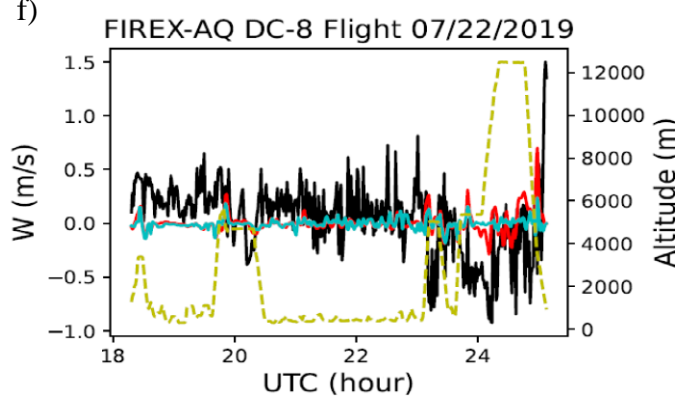
PM2.5 ($\mu g/m^3$)
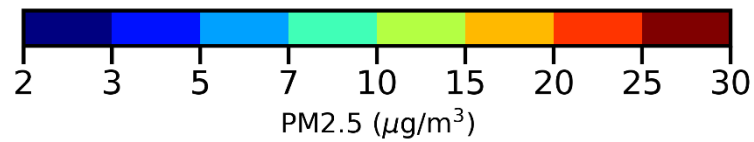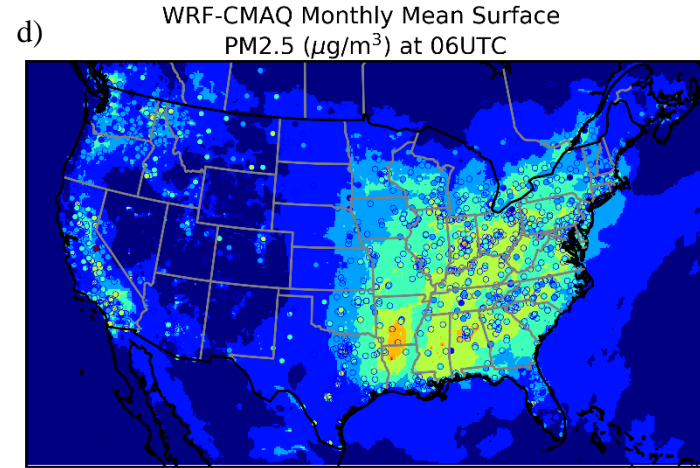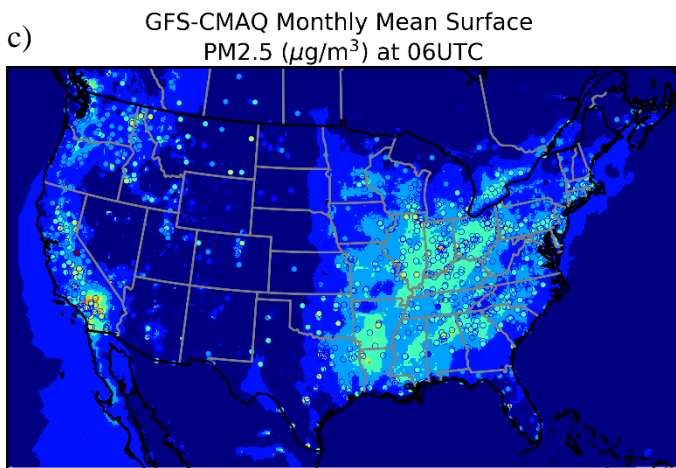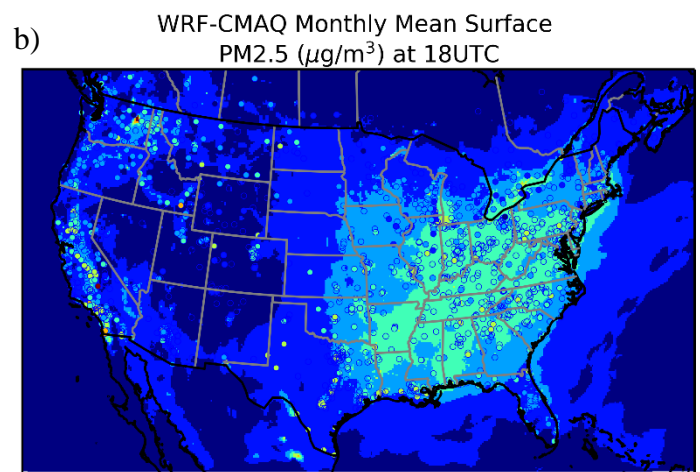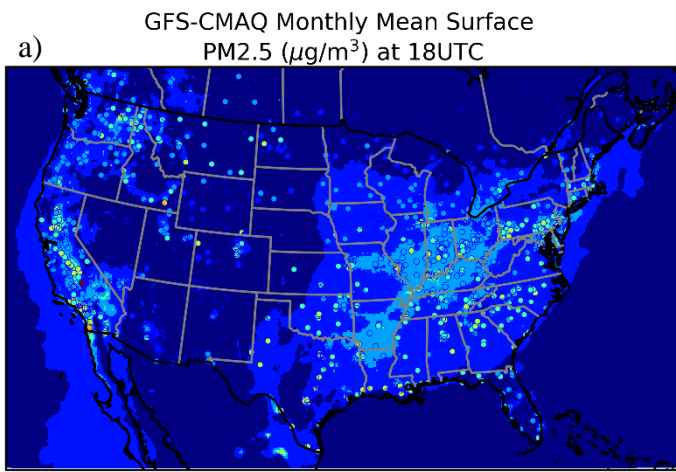
Figure 6, same as figure 5 but for surface PM2.5
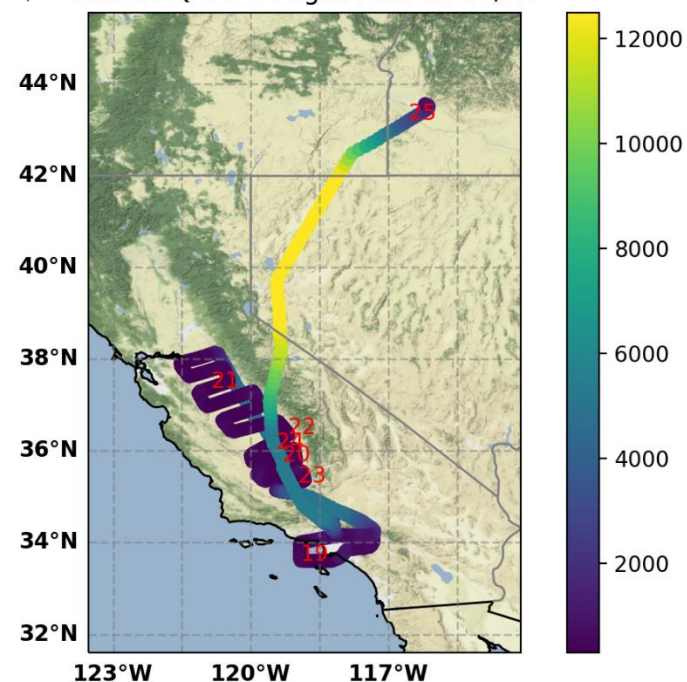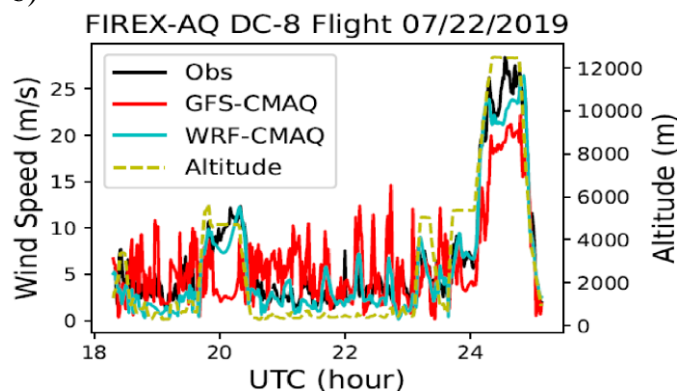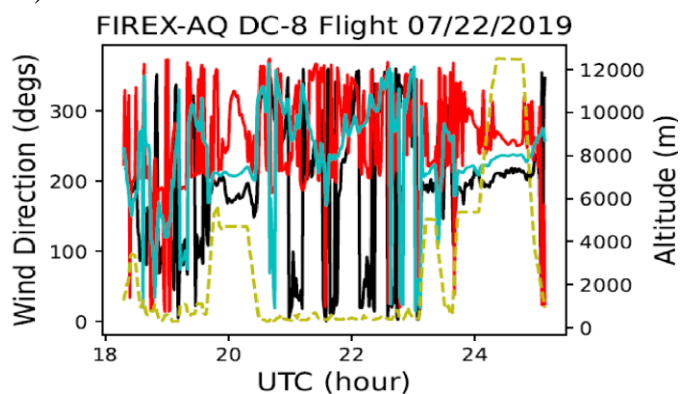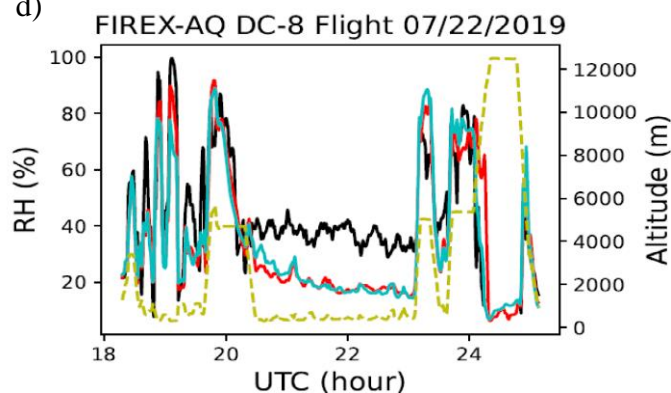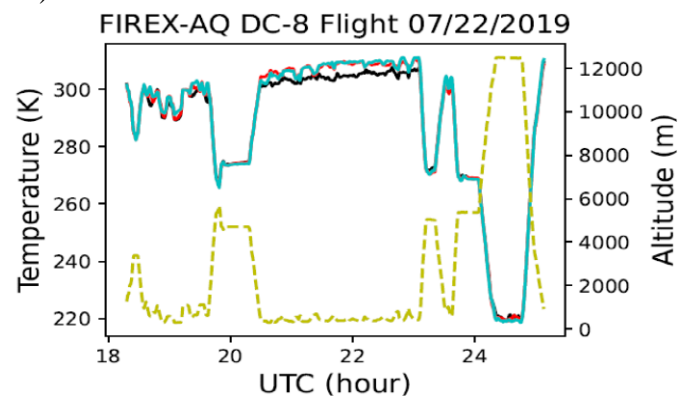
Figure 7. Modeled meteorological variables compared with observations for the DC-8 flight on 22 July, 2019 (b to f). The plot a shows the flight path colored in altitudes above sea level with UTC time in red text. Base map credits: © OpenStreetMap contributors 2022. Distributed under the Open Data Commons Open Database License (ODbL) v1.0.

37

a) GFS-CMAQ predicted vertical velocity along the DC-8 flight path, 22, July, 2019
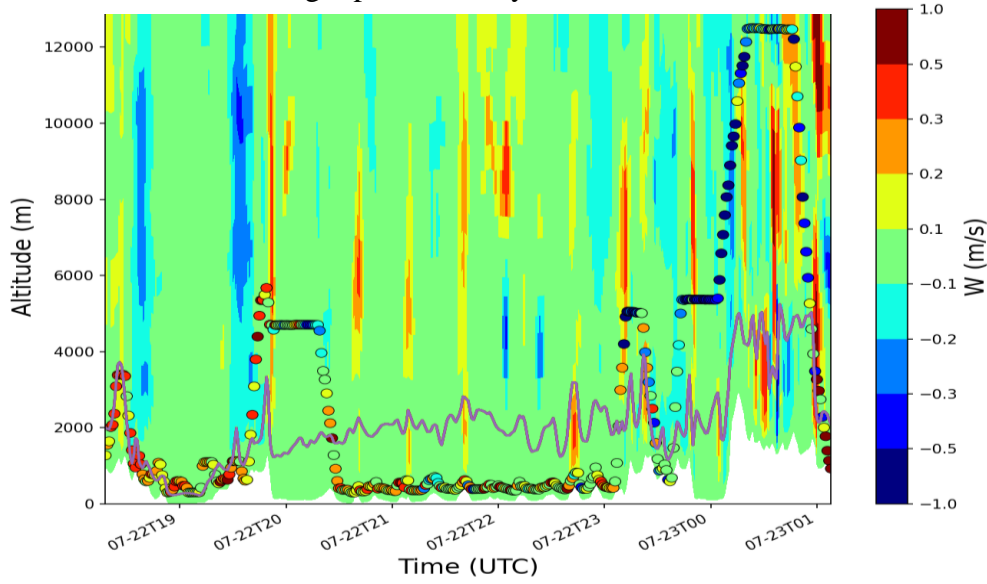
b) WRF-CMAQ predicted vertical velocity along the DC-8 flight path, 22, July, 2019
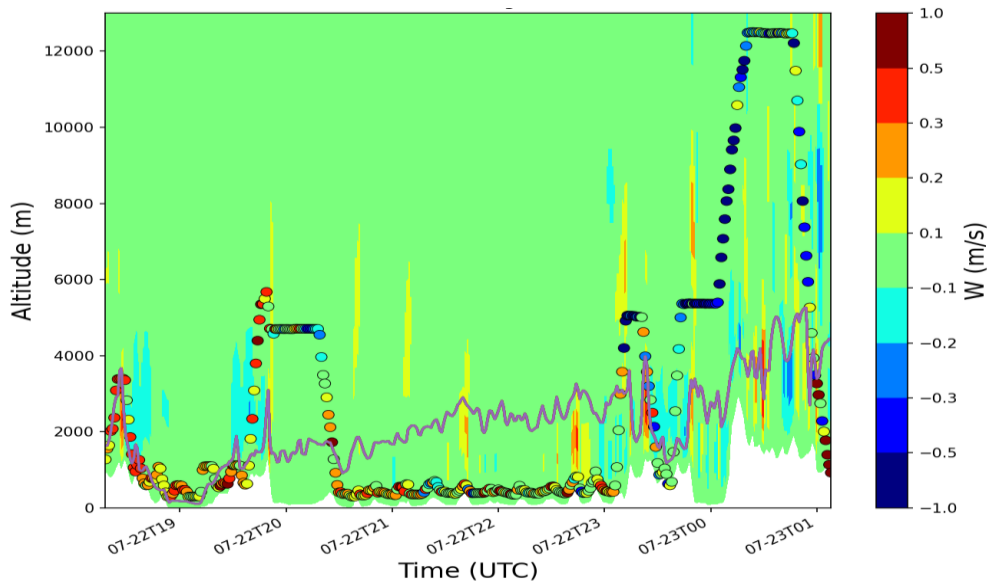

Figure 8, Curtain plots of the vertical velocity (W) predicted by GFS-CMAQ (a) and WRF-CMAQ (b) along the DC-8 flight on 22 July, 2019. The colored dots showed the DC-8 measured vertical velocities. The solid lines showed the predicted PBL heights of these two models.
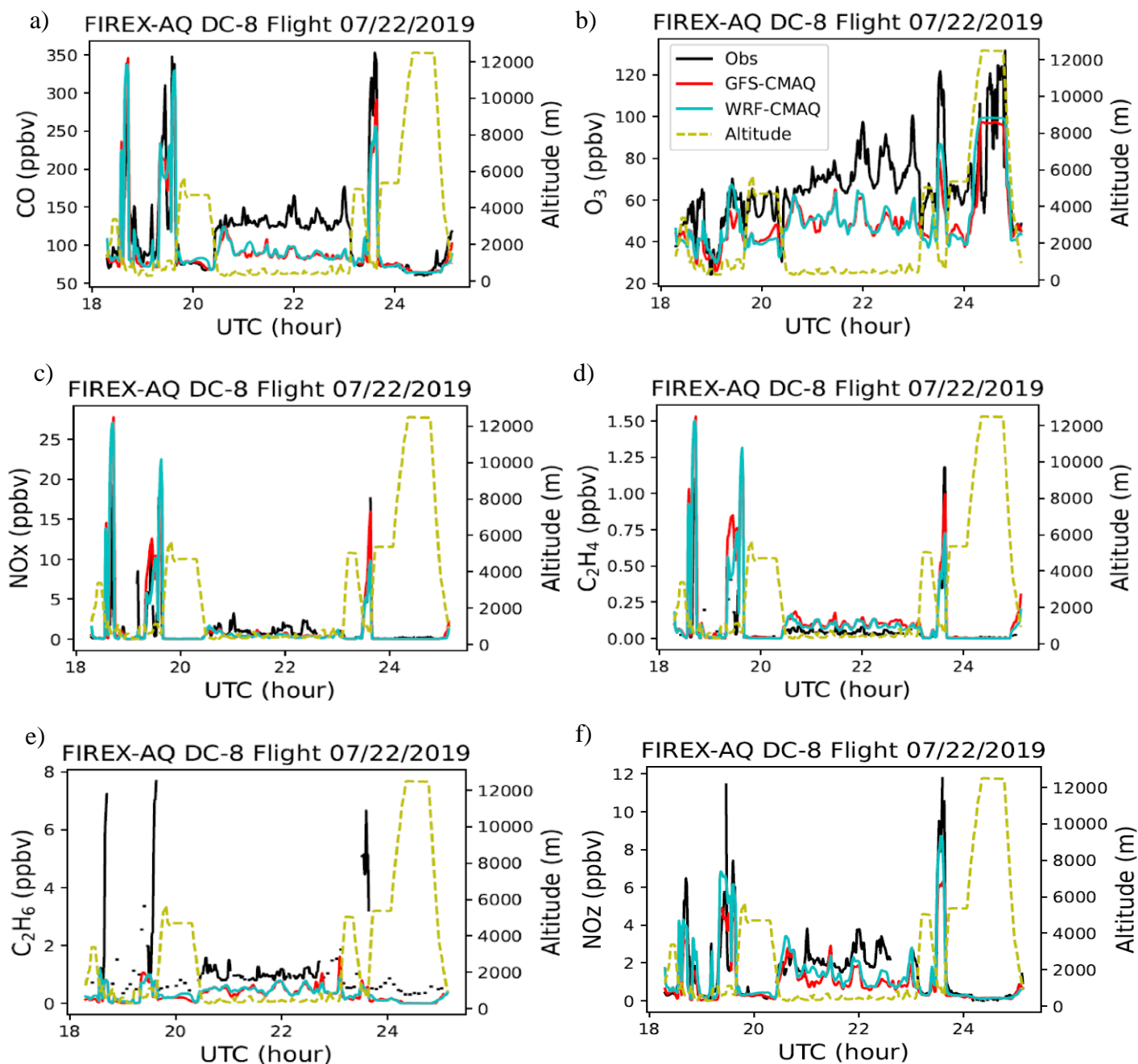
Figure 9. Model predicted chemical concentrations compared with observations along with the DC-8 flight on 22 July, 2019
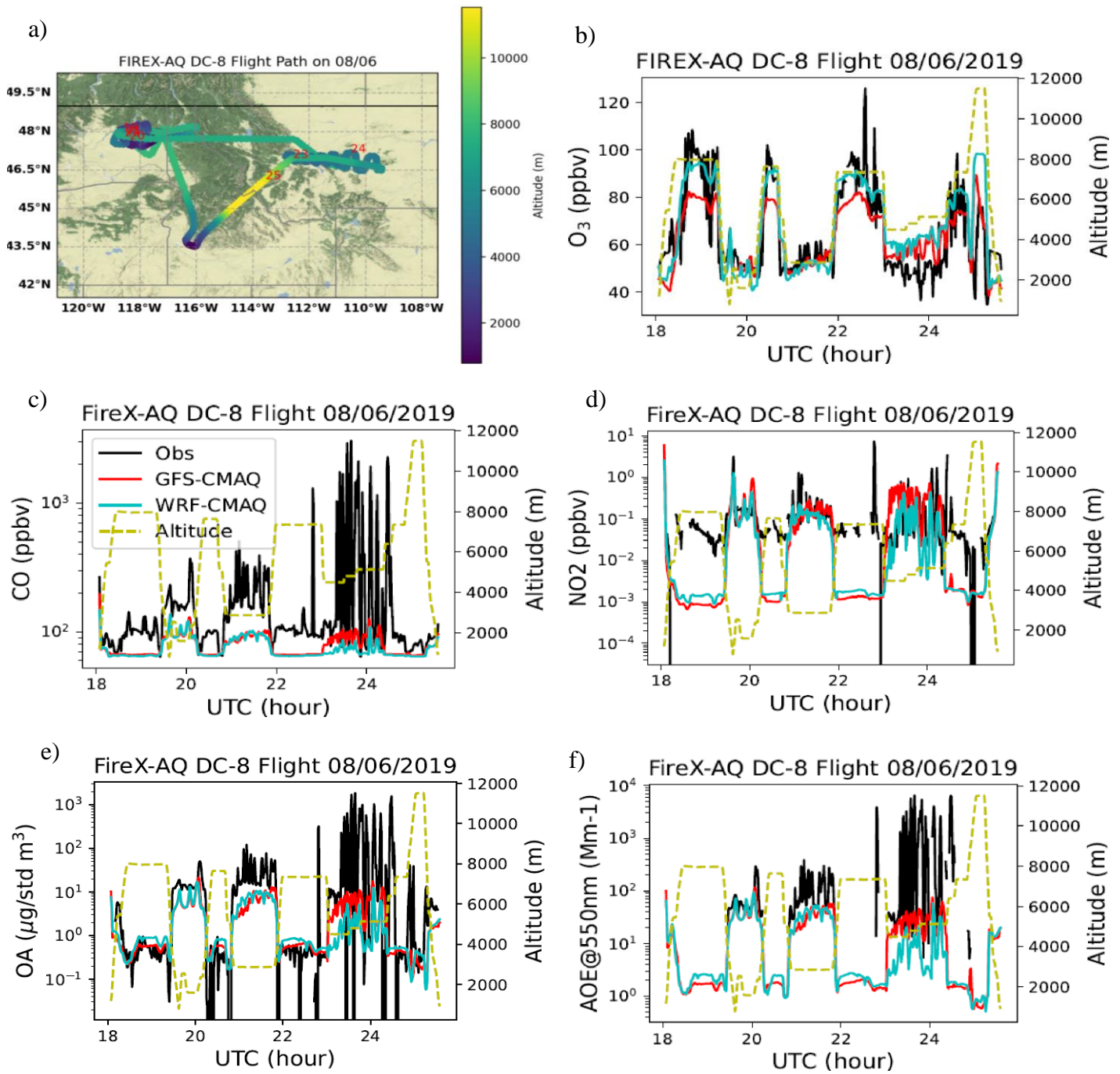
Figure 10. The DC-8 flight path (a), and model-observation comparisons for O_3 (b), CO (c), NO_2 (d), submicron organic aerosol (OA) (e) and aerosol optical extinction coefficient (AOE) at wavelength of 550nm (f) on 06 August, 2019. Base map credits: © OpenStreetMap contributors 2022. Distributed under the Open Data Commons Open Database License (ODbL) v1.0.

a) DIAL-HSRL aerosol backscatter coefficient (ABC) at 532nm wavelength along the DC-8 flight path, 6 Aug., 2019

b) DIAL-HSRL cloud screened ABC at 532nm wavelength along the DC-8 flight path, 6 Aug., 2019

c) GFS-CMAQ predicted AOE@550nm (/Mm) along the DC-8 flight path, 6 Aug., 2019

d) WRF-CMAQ predicted AOE@550nm (/Mm) along the DC-8 flight path, 6 Aug., 2019

e) GFS-CMAQ predicted RH (%) along the DC-8 flight path, 6 Aug., 2019

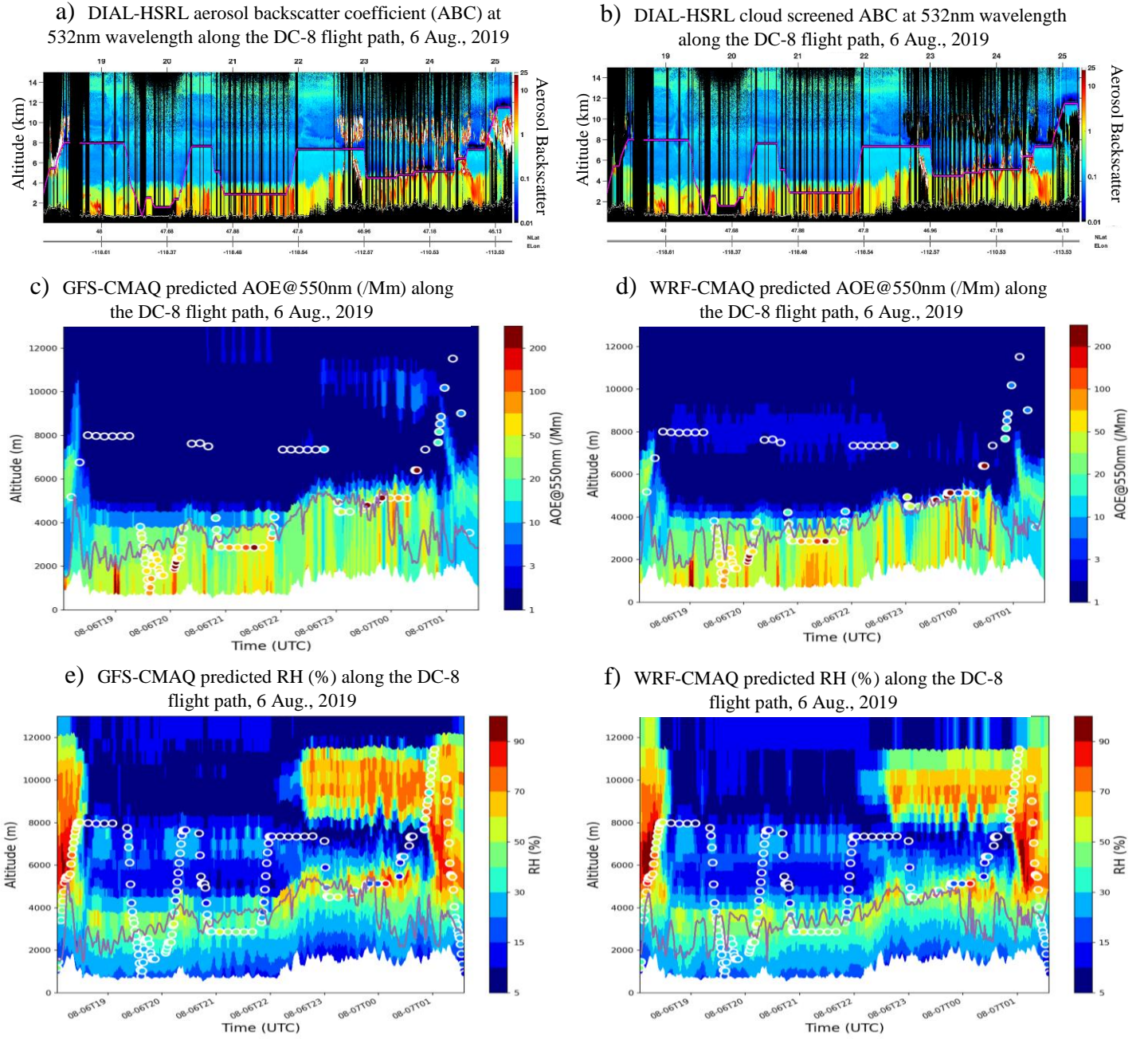f) WRF-CMAQ predicted RH (%) along the DC-8 flight path, 6 Aug., 2019

Figure 11, The Differential Absorption High Spectral Resolution Lidar (DIAL-HSRL) retrieved aerosol backscatter coefficient (ABC) at 532nm wavelength in unit /km/steradian (a) and cloud screened one (b); curtain plots of the AOE (b, c) and relative humidity (RH) (d, e) predicted by GFS-CMAQ (left) and WRF-CMAQ (right) along the DC-8 flight on 06 August, 2019. The colored dots showed the corresponding measured values. The solid lines showed the predicted PBL heights of these two models.